Structures 79 (2025) 109423

Contents lists available at ScienceDirect

Structures

journal homepage: www.elsevier.com/locate/structures

Nondestructive evaluation of hybrid concrete properties using image processing and machine learning

Vagelis Plevris[a,*,1], Ammar T. Al-Sayegh[b,2], Junaid Mir[c,3], Afaq Ahmad[d,4]

[a] Department of Civil and Environmental Engineering, College of Engineering, Qatar University, Qatar
[b] Department of Civil Engineering, College of Engineering & Petroleum, Kuwait University, Kuwait
[c] Department of Electrical Engineering, University of Engineering & Technology Taxila, Pakistan
[d] Department of Building and Energy Engineering, Oslo Metropolitan University, Norway

ARTICLE INFO

Keywords:
Machine learning
Image processing
Hybrid concrete
Cement replacement materials
Silica fume
Fly ash

ABSTRACT

Advancements in informatics, such as image processing (IP) and machine learning (ML), are increasingly being utilized to evaluate the mechanical properties of reinforced concrete structures. This study focuses on hybrid concrete (HC), which incorporates cement replacement materials (CRM) like fly ash and silica fume to enhance its mechanical performance while promoting sustainability. A novel methodology combining IP with supervised ML models—Support vector machine (SVM), boosted ensemble regression (BRE), and Gaussian process regression (GPR)—was developed to predict the compressive and tensile strengths of HC. A comprehensive dataset was created using 162 cylindrical specimens prepared with various mix ratios, CRM replacement levels, and curing durations. High-resolution images of both horizontal and vertical cuts of the specimens were analyzed, and statistical features were extracted to train the ML models. The results demonstrated the models' high accuracy in predicting mechanical properties, with GPR emerging as the most reliable method. The findings confirm the effectiveness of integrating IP with ML as a nondestructive testing approach for concrete evaluation, offering a fast, cost-effective, and environmentally friendly alternative to traditional methods. This study underscores the potential of combining advanced computational techniques with sustainable materials to innovate in concrete technology.

1. Introduction

Over the past few decades, image processing (IP) and machine learning (ML) algorithms have been widely applied to address complex challenges across various scientific and technological fields. In civil engineering, these advanced methods have gained prominence as alternative solutions for issues related to structural health monitoring (SHM) and concrete technology [1–3]. SHM involves the continuous assessment of structural conditions to enable preventive measures against potential damage or failure [4]. This process requires regular monitoring of key physical parameters that indicate a structure's health, providing quantifiable insights into its current state. Critical physical quantities, such as material properties, accelerations, displacements, and strains, are measured to evaluate the condition of civil structures [5, 6]. However, obtaining accurate measurements of these parameters poses significant challenges. The process is often complex, requiring

---

Abbreviations: AI, Artificial Intelligence; ANFIS, Adaptive Neuro-Fuzzy Inference System; ANN, Artificial Neural Network; BRE, Boosted Ensemble Regression; CRM, Cement Replacement Material; DT, Decision Tree; FA, Fly Ash; f_c, Compressive Strength; f_t, Tensile Strength; GPR, Gaussian Process Regression; HC, Hybrid Concrete; IP, Image Processing; KNN, k-Nearest Neighbors; LOI, Loss on Ignition; ML, Machine Learning; PD, Pixel Distribution; RBF, Radial Basis Function; RC, Reinforced Concrete; RF, Random Forest; RH, Rebound Hammer; SF, Silica Fume; SVM, Support Vector Machine; UPV, Ultrasonic Pulse Velocity; W/C, Water-to-Cement ratio.

* Corresponding author.
E-mail addresses: vplevris@qu.edu.qa (V. Plevris), al.sayegh@ku.edu.kw (A.T. Al-Sayegh), junaid.mir@uettaxila.edu.pk (J. Mir), afaq.ahmad@oslomet.no (A. Ahmad).

[1] ORCiD ID: 0000-0002-7377-781X
[2] ORCiD ID: 0000-0002-0334-5413
[3] ORCiD ID: 0000-0002-4587-5121
[4] ORCiD ID: 0000-0001-9427-4296

https://doi.org/10.1016/j.istruc.2025.109423
Received 19 December 2024; Received in revised form 24 May 2025; Accepted 10 June 2025

specialized expertise, and is also time-consuming, labor-intensive, and expensive. Furthermore, the accuracy of these measurements depends heavily on the skill and experience of the individuals performing the monitoring, introducing variability and potential subjectivity into the evaluation.

Concrete is the most widely used construction material globally, offering numerous advantages over other building materials, including durability, strength, cost-effectiveness, and modularity. It comprises a mixture of blended cement, coarse and fine aggregates, sand, and water. Concrete plays a critical role in the stability of reinforced concrete (RC) structures, making it essential to study its mechanical properties to understand its quality and behavior under load better [7,8]. Among these properties, compressive strength (f_c) and split-tensile strength (f_t) are particularly significant due to their direct impact on structural safety and concrete performance evaluation. Given its composition of various components in different proportions, concrete exhibits a complex anatomy, with its properties strongly influenced by its constituents [9, 10]. As a result, accurately determining its mechanical characteristics presents a challenge.

Cement replacement materials (CRM) are frequently incorporated into concrete mixtures, offering several benefits, including enhanced strength, reduced CO_2 emissions, and cost efficiency. Silica fume (SF) and fly ash (FA) are among the most commonly used CRMs in the concrete industry [11]. These pozzolanic waste materials react with water to produce calcium silicate hydrate gel, which acts as a binder and improves the mechanical properties of concrete. Additionally, the microparticles of SF and FA fill voids between aggregates, reducing air pockets and further enhancing concrete properties [10,12,13]. Liu et al. [14] investigated the impact of SF on the mechanical properties of ultra-high-performance concrete at varying volume fractions (5 %, 10 %, 20 %, and 30 %). The study found that incorporating SF significantly improved mechanical characteristics, though its effect on concrete workability was not linear. Other studies have observed that FA negatively affects mechanical properties in the early stages due to its slower pozzolanic reaction but contributes to strength development over time. Conversely, SF consistently enhances concrete properties across all ages [10,15,16].

Accurately measuring f_c and f_t is essential given the critical role of concrete's mechanical properties in building stability [17,18]. Destructive testing has been the most direct method for determining f_c and f_t of concrete [19,20]. This typically involves preparing standard-sized cylindrical or cubic concrete samples with varying water-to-cement (W/C) ratios, aggregate quantities, sand content, CRM proportions, and curing ages to achieve the desired strength. These specimens are then subjected to crushing in a laboratory using a uniaxial compression machine to measure f_c [21] and f_t [22–24]. However, destructive testing methods are costly, time-consuming, and less suitable in the modern era with the advent of nondestructive testing (NDT) techniques [25]. NDT methods address the challenge of assessing the current condition of concrete in existing structures, offering an alternative to destructive approaches. Commonly used NDT techniques include ultrasonic pulse velocity (UPV) and rebound hammer (RH) tests, which are employed to estimate f_c both in the laboratory and in-situ. The UPV test relates f_c to the measured velocity, while the RH test uses the R-value as an indicator [19]. However, these correlations are theoretically complex, with both velocity and R-value influenced by factors such as the W/C ratio, CRM content, structural member type, and test conditions [26]. As a result, these methods, while promising, are susceptible to variability and may lack the precision required for highly accurate measurements [27]. NDT methods can be combined with core cutting or partially destructive testing to improve reliability. Nevertheless, traditional NDT methods are generally inadequate for accurately determining concrete's mechanical properties.

With advancements in computer technology, ML algorithms, and IP techniques have become powerful tools for measuring concrete properties. ML, a branch of artificial intelligence (AI), is widely used for regression, clustering, and classification tasks. Models like decision trees (DT), boosted ensemble regression (BRE), Support vector machines (SVM), Gaussian process regression (GPR), and random forests (RF) offer significant advantages over traditional regression techniques. These models learn patterns from input data and provide highly accurate predictions for output data, making them particularly effective for estimating the mechanical properties of concrete [20,28–31]. In addition, IP techniques have been applied to various aspects of concrete analysis, including measuring crack features [32], predicting concrete properties [33], detecting cracks [34], quantifying bug holes [35], and analyzing the interfacial transition zone in concrete [36]. For instance, Ahmad et al. [37] employed supervised ML models to estimate the strength of concrete at elevated temperatures. Asteris et al. [38] utilized surrogate ML models to predict f_c, while Kang et al. [39] applied ML to predict both f_c and f_t in silica fume-incorporated steel fiber-reinforced concrete. Their study employed 11 ML algorithms with k-fold cross-validation to prevent overfitting.

Başyiğit et al. [40] utilized IP techniques to evaluate the f_c of concrete. Concrete cube specimens were sectioned and photographed in a controlled environment to capture internal details. RGB-mode photographs were converted to grayscale, enabling pixel value extraction for each concrete component through thresholding and histogram analysis. By correlating these pixel values with the actual volumes of concrete constituents, f_c was estimated using IP-derived information. Dogan et al. [41] employed three statistical features—average, median, and standard deviation—from concrete images to predict f_c, maximum deformation, and modulus of elasticity using artificial neural networks (ANN). Another study [42] combined IP and ANN as a nondestructive method to estimate f_c, demonstrating the potential of image features to establish strong relationships with concrete's physical properties [41,42]. Peng et al. [43] applied digital IP techniques to analyze mesoscale fractures in recycled aggregate concrete. Ghanizadeh et al. [44] used SVM and ANN to predict the f_c of plastic concrete, finding these algorithms highly effective for strength estimation. Feng et al. [20] employed an adaptive boosting ensemble technique to improve the accuracy of f_c predictions by building robust learners from weak ones.

Zhang et al. [45] used ML algorithms to predict various mechanical properties of concrete, including f_c, f_t, tensile strain, and elastic modulus. The BRE model offered superior prediction accuracy, robustness, and parameter measurement capabilities. Ahmad et al. [28] also achieved high accuracy in estimating f_c using an ensemble algorithm, validating the model's performance through k-fold cross-validation. Koya et al. [46] applied multiple ML techniques—linear regression, SVM, Gaussian processes, DT, RF, and gradient boosting—to estimate various physical properties of concrete, including Poisson's ratio, f_c, f_t, modulus of elasticity, thermal expansion coefficient, and rupture modulus. Their comparative study highlighted the SVM model as the most accurate among the tested algorithms. Zhang and Xu [47] used GPR to predict concrete's f_c, f_t porosity, and density, noting its precision, stability, and robustness. Yetilmezsoy et al. [48] employed GPR, SVM, and DT with different kernels to approximate the lateral confinement factor of CFRP (carbon fiber reinforced polymer) wrapped RC columns. Basaran et al. [49] estimated the bond strength of FRP (fiber-reinforced polymer) concrete using GPR, SVM, ANN, DT, and multiple linear regression, demonstrating the effectiveness of these techniques in predicting concrete properties.

The primary objective of this study is to estimate the mechanical properties of hybrid concrete using statistical image features and ML models. Three supervised learning models—SVM, BRE, and GPR—were employed to predict concrete properties based on six statistical features extracted from concrete images. To create the dataset, 162 cylindrical concrete specimens were prepared with mix ratios of 1:3:6, 1:2:4, and 1:1.5:3, using varying W/C ratios (0.4, 0.5, 0.6), cement dosages, aggregate quantities, sand content, and CRM percentages (0 %, 15 %, 25 %). The curing times were set at 14 and 28 days. SF and FA were used as CRMs, replacing cement by weight at the specified percentages. The specimens were divided into three equal groups (54 specimens each). One group was tested for f_c, another for f_t, and the third was sectioned into six slices (three horizontal and three vertical) per specimen, yielding 324 slices. These slices were photographed, and MATLAB was used to extract six statistical features—mean, median, standard deviation, skewness, entropy, and third moment—from the images. The extracted statistical features and f_c and f_t values formed the dataset for training and testing the ML models. These models were evaluated for their ability to predict hybrid concrete's mechanical properties accurately. The methodology is briefly described schematically in Fig. 1.

The present work is an extension of a previous study by the authors [50]. In the earlier work, the focus was solely on images derived from horizontal cuts of the concrete specimens, limiting the analysis to a single plane. In contrast, the current study incorporates both horizontal and vertical cut images, providing a more comprehensive perspective to investigate the distribution and effects of CRM throughout the concrete cylinder. Furthermore, while the previous study employed only two supervised learning models—Artificial Neural Network (ANN) and Adaptive Neuro-Fuzzy Inference System (ANFIS)—to predict the mechanical properties of concrete, this work utilizes three distinct supervised learning models, namely SVM, BRE, and GPR, to enhance predictive accuracy and reliability.

2. Overview of image processing and machine learning algorithms

Image processing involves the application of computer algorithms to analyze and modify images, extracting relevant information for various purposes. This field employs tools such as MATLAB, ImageJ, and specialized Python libraries to process images across multiple domains [1,51–53]. A fundamental technique in IP is digitalization, which transforms an image into a digital form. Each element corresponds to a pixel in a digitized image, representing visual data as a matrix. In a grayscale image, a pixel, the smallest unit of an image, contains information about the brightness or intensity of a specific area [41]. Key techniques in IP include segmentation, classification, pattern recognition, digitalization, and image quality enhancement. These methods enable the interpretation and analysis of images for diverse applications. For instance, IP is used in biology and medicine to evaluate biomedical images, in engineering and physics to process spectrometry, and in aeronautics and aerospace to analyze satellite imagery [54].

Supervised ML techniques rely on labeled data to learn relationships between inputs and outputs, enabling them to perform tasks such as regression and classification. These algorithms are capable of recognizing patterns, learning from past examples, and making informed predictions on new, unseen data. By using these learning capabilities, supervised ML models can generalize from training data to accurately estimate outcomes in complex datasets. Numerous ML models, including GPR, BRE, SVM, and others, are available for these purposes. Among them, SVM is a sophisticated supervised learning model used in ML. It operates on the principles of statistical learning theory and structural risk minimization. SVM effectively maps input data from a training dataset into a high-dimensional feature space with precision, enabling accurate predictions. A crucial factor in the practical training and precision of SVM in regression tasks is the choice of the kernel function. Commonly used kernel functions in SVM include the radial basis function (RBF), polynomial kernel, sigmoid kernel, and linear kernel. The performance of the SVM model significantly depends on the selected kernel function. Studies have shown that the RBF kernel typically provides a higher degree of accuracy compared to other kernel functions used in SVM [55,56].

BRE is a popular model within the ensemble learning category of ML, used for both regression and classification tasks. BRE is based on the principles of learning theory, aiming to improve prediction accuracy iteratively. The process begins by training an initially weak learner using the given data. After evaluating the prediction accuracy of this learner, the training data distribution is adjusted for the next weak learner, with greater emphasis placed on data points where the previous learner performed poorly. By assigning varying weights to weak learners, BRE enhances overall accuracy, transforming the weak learners into a robust predictive model [20,57].

GPR is a nonparametric supervised ML technique capable of modeling complex relationships between input and target variables. GPR defines a prior probability distribution over a latent function, allowing for flexibility in capturing intricate patterns. The number of optimizable variables in GPR increases with the size of the dataset, making it well-suited for both small and large datasets in regression tasks. Additionally, the predictive performance of GPR can be enhanced by employing various kernel functions, such as exponential, squared exponential, Matérn32, Matérn52, and rational quadratic kernels [58].

3. Dataset generation

This section outlines the methodology used to construct the dataset by integrating statistical features extracted from concrete images with target values obtained through laboratory testing. It includes a description of the materials and mix proportions used in preparing the cylindrical concrete specimens, as well as a detailed explanation of the image acquisition process.

3.1. Specimen preparation

This study involved casting 162 cylindrical concrete specimens, each with a diameter of 150 mm and a height of 300 mm, to examine the factors influencing the ultimate mechanical properties of concrete. The investigation focused on six key factors: mix ratio, W/C ratio, aggregate

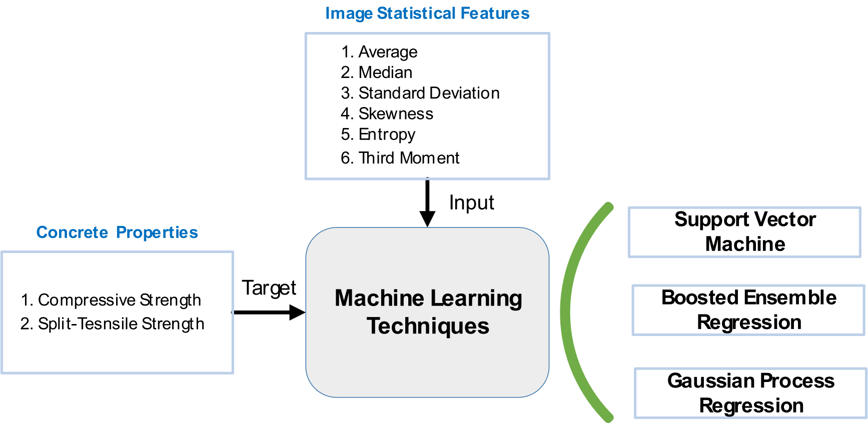

Fig. 1. Schematic diagram of the adopted methodology.

content, compaction technique, curing duration, and the inclusion of CRM, as summarized in the flowchart in Fig. 2. The W/C ratio, a critical parameter in concrete production, significantly affects concrete's surface finish and void content. To study these effects, three W/C ratios (0.4, 0.5, and 0.6) were used for specimen preparation, following ASTM C94 [59] and ACI 318 [60] Standards for water quality. Additionally, three different cement dosages were selected to evaluate the impact of cement content on concrete color variation.

Table 1 presents the chemical composition of the pozzolanic materials used in this study, including cement, SF, and FA. The table highlights the variation in key chemical components among these materials, directly influencing their pozzolanic activity and impact on concrete properties. Loss on Ignition (LOI) is the percentage of weight loss that appears when a material is heated to a definite high temperature, typically around 950–1000°C, under controlled conditions. This weight loss reveals the sample's volatile substances (such as water, carbon dioxide, and organic compounds) and combustible materials. LOI is a crucial parameter in quality control and material characterization for cementitious materials. Cement has the lowest LOI value at 0.64 %, indicating minimal volatile content and high purity, which is essential for consistent hydration and strength development in concrete. SF exhibits a higher LOI range of 4–7 %, reflecting the presence of minor organic impurities or absorbed moisture. FA shows the highest LOI value at 9.01 %, which can be attributed to unburned carbon or other volatile components from its production as a byproduct of coal combustion.

Table 1
Chemical composition of cement, silica fume, and Fly ash.

	Silica (%)	Aluminum oxide (%)	Iron oxide (%)	Calcium oxide (%)
Cement	22.5	5	4.0	64.25
Silica Fume	84–86	1.0 (max)	2.0–3.5	1.0–1.5
Fly Ash	57–65	28–32	1–4	1–2

Table 2 categorizes the specimens into three groups based on CRM percentages. Each mix ratio, referring to the Cement: Fine: Coarse Aggregate ratio (by weight), was assigned a unique identifier, such as *10S0.4 W14D*, where *10S* represents the total mix ratio components (1 +3 +6 =10), *0.4 W* denotes the W/C ratio (0.4), and *14D* indicates the curing duration in days (14). CRM, is known to enhance the fluidity of concrete mixes and reduce void ratios per ASTM C31 [61], was added to 54 of the 81 total specimens. FA and SF were used as CRMs to replace 0 %, 15 %, and 25 % of the cement by weight. Equal quantities of FA and SF were used in each case; for example, 15 % CRM means 15 % FA and 15 % SF as substitutes for cement.

3.2. *Image acquisition setup*

Photographs of the prepared concrete slice samples were taken in a purpose-built room measuring 2.00 m by 2.50 m. Given the significant impact of image quality on the effectiveness of IP techniques, the photography setup was fully controlled. Measures were taken to ensure consistency in noise, lighting, and shadow levels across all images. To

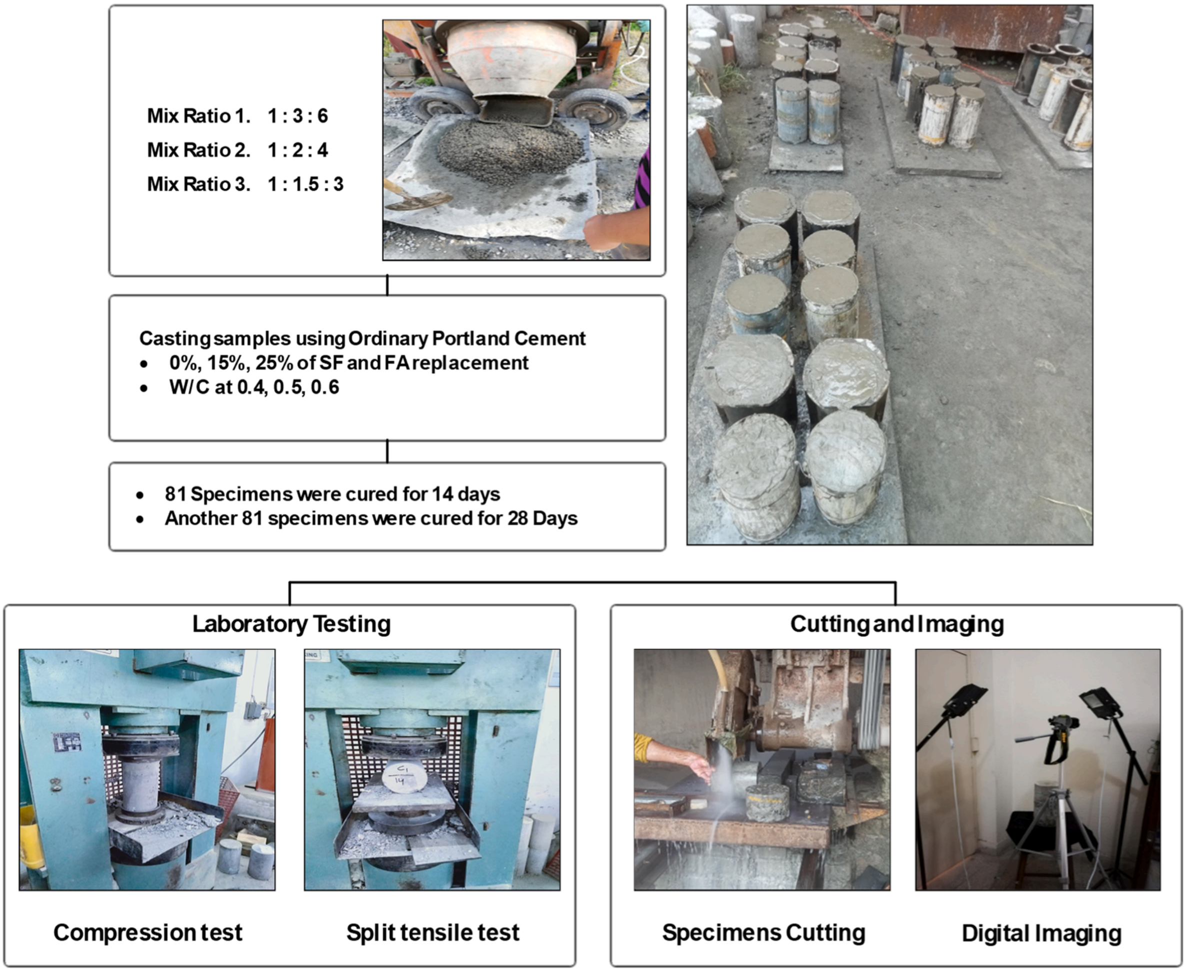

Fig. 2. Overview of the experimental workflow, including concrete mixing, specimen casting and curing, compressive and tensile strength testing, specimen cutting, and controlled image acquisition setup for digital analysis.

Table 2
Details of specimens mix ratio, CRM and curing.

Sample Code	Mix Ratio	W/C Ratio	Curing Period (days)
10S0.4W14D	1: 3: 6	0.4	14
10S0.5W14D	1: 3: 6	0.5	14
10S0.6W14D	1: 3: 6	0.6	14
7S0.4W0C	1: 2: 4	0.4	14
7S0.5W14D	1: 2: 4	0.5	14
7S0.6W14D	1: 2: 4	0.6	14
5.5S0.4W14D	1: 1.5: 3	0.4	14
5.5S0.5W14D	1: 1.5: 3	0.5	14
5.5S0.6W14D	1: 1.5: 3	0.6	14
10S0.4W28D	1: 3: 6	0.4	28
10S0.5W28D	1: 3: 6	0.5	28
10S0.6W28D	1: 3: 6	0.6	28
7S0.4W28D	1: 2: 4	0.4	28
7S0.5W28D	1: 2: 4	0.5	28
7S0.6W28D	1: 2: 4	0.6	28
5.5S0.4W28D	1: 1.5: 3	0.4	28
5.5S0.5W28D	1: 1.5: 3	0.5	28
5.5S0.6W28D	1: 1.5: 3	0.6	28

block sunlight, black sheets were used to cover all room openings. Artificial lighting was provided by two 30 W LED bulbs positioned at specific angles to illuminate the concrete slices uniformly [41]. A lux meter (Lutron LX 1109) measured the light intensity, ensuring consistent illumination and minimizing unwanted shadows. The images were captured using a Nikon 3300 DSLR camera with a resolution of 24 megapixels. The camera's ISO setting, which determines its sensitivity to light, was fixed at 1000. To maintain uniformity, the camera was mounted on a stand directly above the samples, with a fixed distance of 60 cm between the camera lens and the surface of each slice. The resulting images had a resolution of 6000 × 4000 pixels, ensuring high-quality visuals suitable for IP.

3.3. *Imaging of concrete specimens*

For photographic analysis, 54 specimens were selected, with one representative sample from each category. The cutting process, illustrated schematically in Fig. 3, was performed in two stages. Initially, two horizontal cuts divided each specimen into three slices. Subsequently,

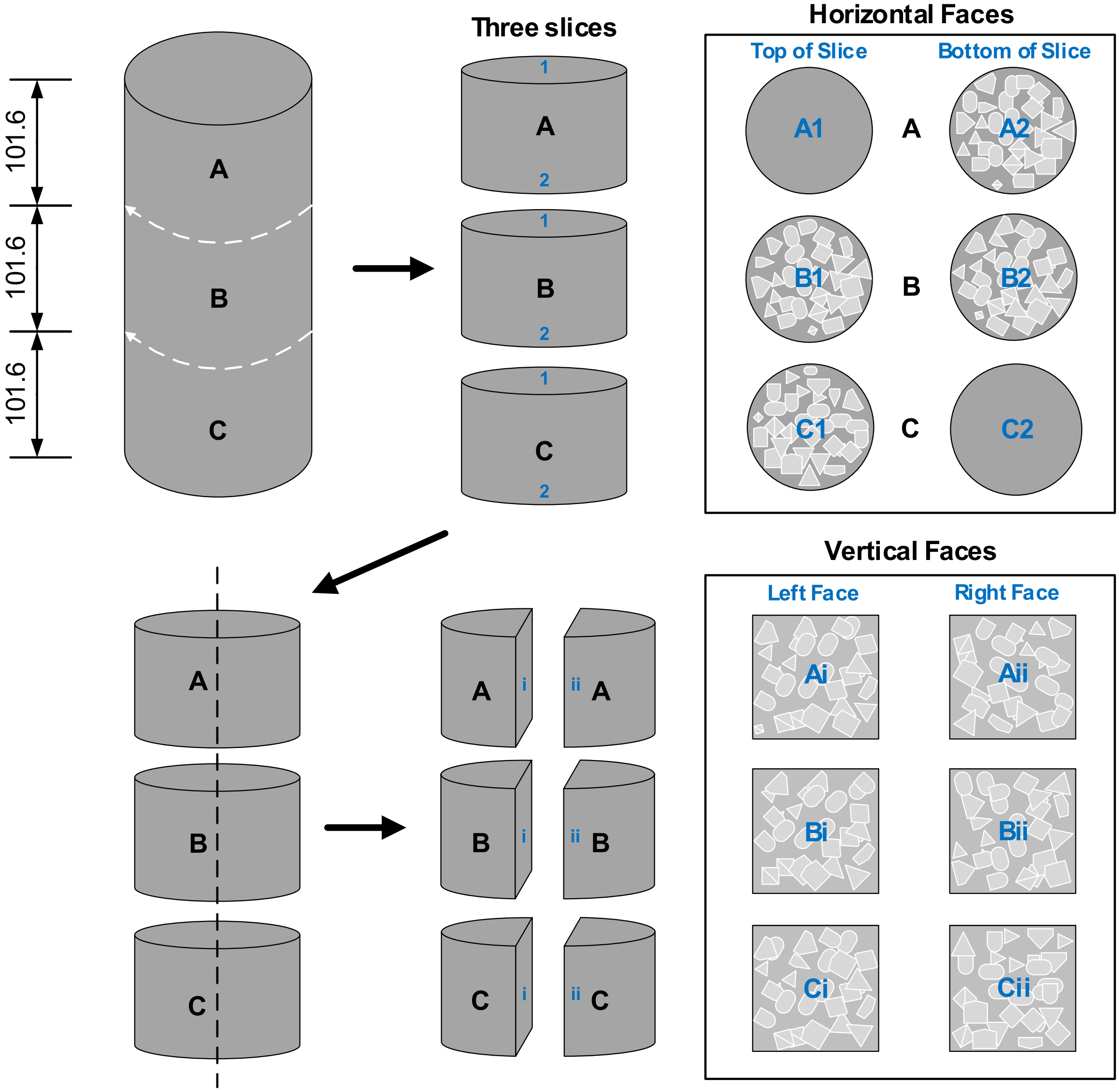

Fig. 3. Schematic diagram of transforming concrete specimen into horizontal and vertical faces.

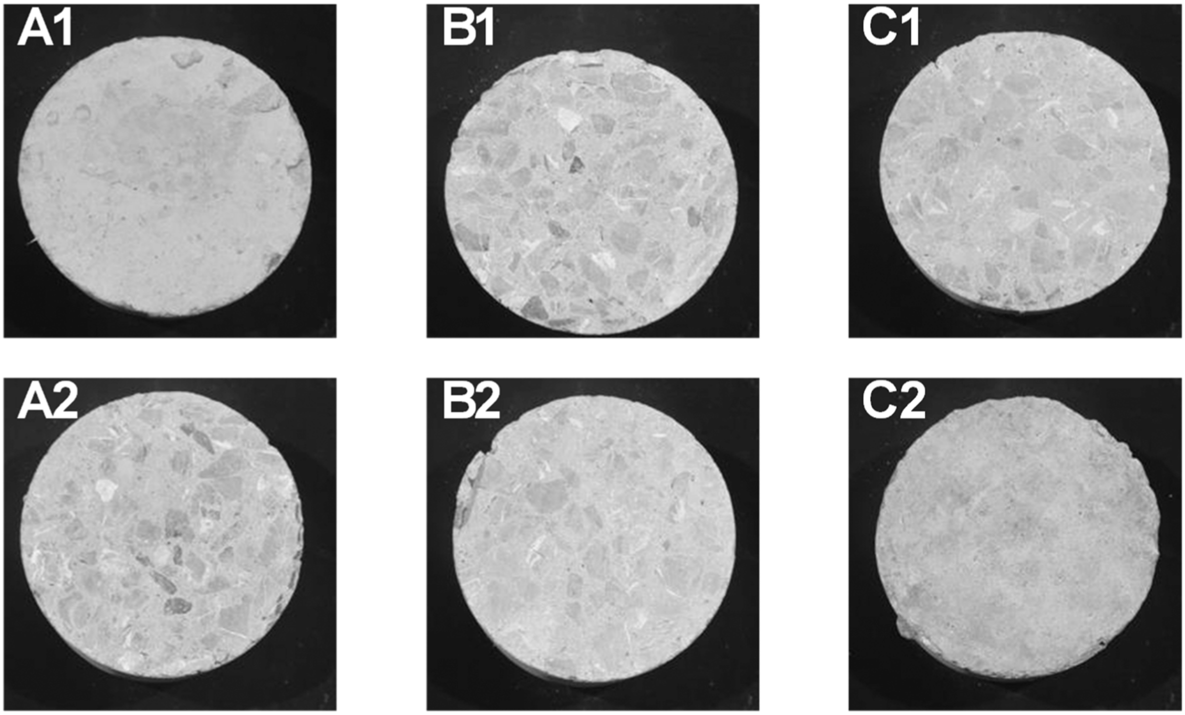

Fig. 4. Faces of concrete slices obtained from horizontal cutting.

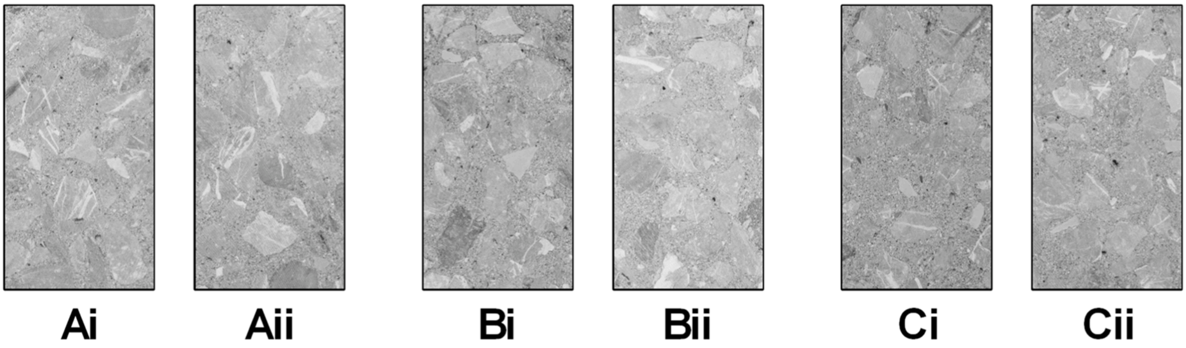

Fig. 5. The faces of concrete slices were obtained from vertical cutting.

vertical cuts were made to split each horizontal slice into two parts, resulting in six distinct vertical faces per specimen. This segmentation allowed for a detailed study of how aggregate distribution affects the mechanical properties of concrete.

Relying solely on images of the top surface without cutting the specimens could lead to inaccurate conclusions, as fine materials often accumulate on the upper surface of concrete [62,63]. To ensure accurate evaluation, all faces of the sliced samples were examined. This approach provided critical insights into parameters influencing concrete's mechanical properties, including cement paste characteristics, void ratio, and aggregate distribution. An example of the faces of concrete slices obtained from horizontal cutting is presented in Fig. 4. It depicts the six faces of the horizontal cut of each slice of the concrete cylinder. A1 is the top surface of the topmost slice, as illustrated in Fig. 3; A2 is the bottom surface of the topmost slice. Similarly, B1 is the top surface of the middle slice, B2 is the bottom surface of the middle slice, and C1 is the top surface of the bottom slice, with C2 as the bottom surface of this slice.

Fig. 5 illustrates an example of the faces of concrete slices obtained from vertical cutting. It shows the six faces of the vertical cut of each slice of the concrete cylinder. Ai is the left face of the topmost slice, as illustrated in Fig. 3; Aii is the right face of the topmost slice. Similarly, Bi is the left face of the middle slice, Bii is the right face of the middle slice, and Ci is the left face of the bottom slice, with Cii as the right face of this slice, as illustrated in Fig. 3 and Fig. 5.

3.4. *Laboratory testing*

Traditional destructive testing methods were employed to evaluate the mechanical properties of concrete specimens. Compression and split-cylinder tests were conducted on the hardened concrete samples to analyze their behavior under compressive and tensile forces, as illustrated in Fig. 6.

3.4.1. *Compressive and split-tensile strength*

The prepared cylindrical concrete specimens with cement content incorporating CRM, such as FA and SF, were tested for compressive strength. CRM was used to replace 0 %, 15 %, and 25 % of the cement by weight. The f_c of the hardened concrete was determined through a compression test conducted in accordance with ASTM C39 [21], as depicted in Fig. 6(b). There are 18 specimens, one from each category, and for each there are 3 CRM levels, resulting in 54 values of f_c in general. The split-tensile strength test was conducted in accordance with

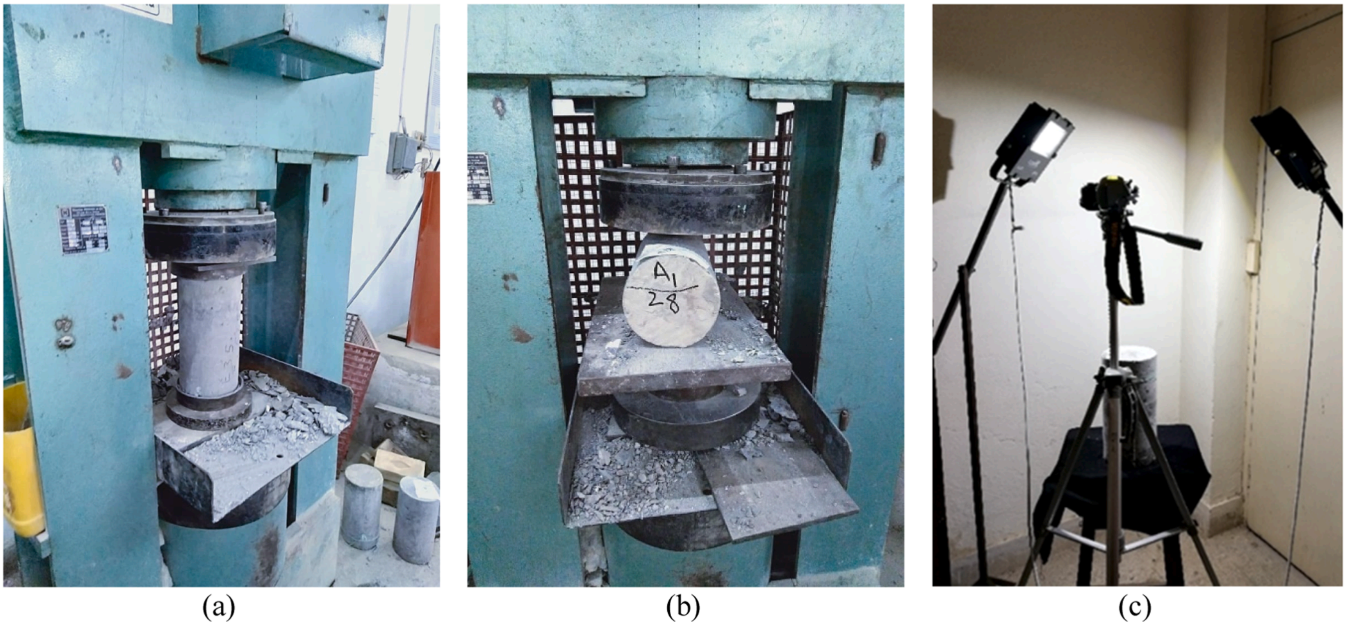
(a) (b) (c)

Fig. 6. Experimental setup for data acquisition: (a) compression test; (b) split-tensile test; (c) imaging.

the ASTM C496 [22] standard, as depicted in Fig. 6(c).

3.5. Statistical feature extraction through image processing

The images of the concrete slice samples were processed using a MATLAB-based IP tool and converted into matrix form with a resolution of 4000 × 6000 pixels. To ensure that only the relevant concrete regions were analyzed, the background was cropped from each image. Originally captured in full color (RGB), the images were then converted to grayscale by applying a weighted combination of the red (R), green (G), and blue (B) channels, as described in Eq. (1).

$$\mathrm{GS} = 0.298 \cdot \mathrm{R} + 0.589 \cdot \mathrm{G} + 0.113 \cdot \mathrm{B} \tag{1}$$

R, G, and B represent a pixel's red, green, and blue color components, and GS is the adjusted grayscale component. The grayscale images were then resized to 256 × 256 pixels. These matrices served as input segments for prediction models, where each pixel value represented the appearance and brightness of specific points in the concrete samples.

Several statistical features—arithmetic mean, standard deviation, median, third moment, skewness, and entropy—were extracted from the grayscale images to enhance the accuracy of predictive models. These features were selected due to their simplicity, computational efficiency, and effectiveness in capturing global intensity distributions. Importantly, these features are inherently rotation-invariant, which supports the generalization of our method across images with varying orientations. In contrast, while texture features, e.g., Haralick descriptors, can capture spatial patterns, they are not inherently rotation-invariant, are more sensitive to noise, and often involve higher computational costs. The selected features provided essential insights into the texture and distribution properties of the concrete samples and were utilized for training ML models [41,64,65]. Table 3 provides a detailed summary of these features and their mathematical expressions can be found in Eqs. (2)-(7) [42].

Table 3
Statistical features from images.

Features	Expression	Description
Mean	M	Measure of average intensity
Median	Me	Middle value of a pixel in an ordered column
Standard deviation	Std	The measure of average contrast
Third moment	Mo	The measure of the distribution skewness
Entropy	E	The measure of randomness in pixels
Skewness	Sk	The measure of asymmetry in matrix

$$CapM = \frac{1}{k}\sum_{i=1}^{k} \mathrm{V}_{\mathrm{i}} \tag{2}$$

$$Me = \{(k+1) \div 2\}^{th} \tag{3}$$

$$Std = \sqrt{\frac{1}{k}\sum_{i=1}^{k} (\mathrm{V}_i - M)^2} \tag{4}$$

$$Mo = \frac{1}{k}\sum_{i=1}^{k} (\mathrm{V}_i - M)^3 \tag{5}$$

$$E = -\sum_{i=1}^{k} \mathrm{c}_{\mathrm{i}} \cdot \log_2(\mathrm{c}_{\mathrm{i}}) \tag{6}$$

$$Sk = \frac{\frac{1}{k}\sum_{i=1}^{k} (\mathrm{V}_{\mathrm{i}} - M)^3}{Std^3} \tag{7}$$

V shows the variable values in the digitized matrix, M denotes their mean value, k is number of values of the variable and Me is the median value. Std denotes the standard deviation, Mo denotes the third moment, c contains the normalized histogram counts, and E is the entropy, while Sk is the skewness value.

To facilitate efficient data handling, the data matrix was further reduced to a size of 6 × 256 (1536 values). This matrix consisted of six rows and 256 columns, with each row corresponding to one of the statistical features—mean, median, standard deviation, third moment, entropy, and skewness, extracted for each sample image. This dimensional reduction preserved critical information for model training and prediction while optimizing data management.

For each specimen, a combined matrix of size 12 × 1536 was constructed, integrating data from twelve images of the concrete sample (see Fig. 4 and Fig. 5). This matrix encompassed 1536 values per specimen, representing the extracted statistical features. Local Binary Patterns (LBP), shown in Fig. 7 and Fig. 8, were derived from images of

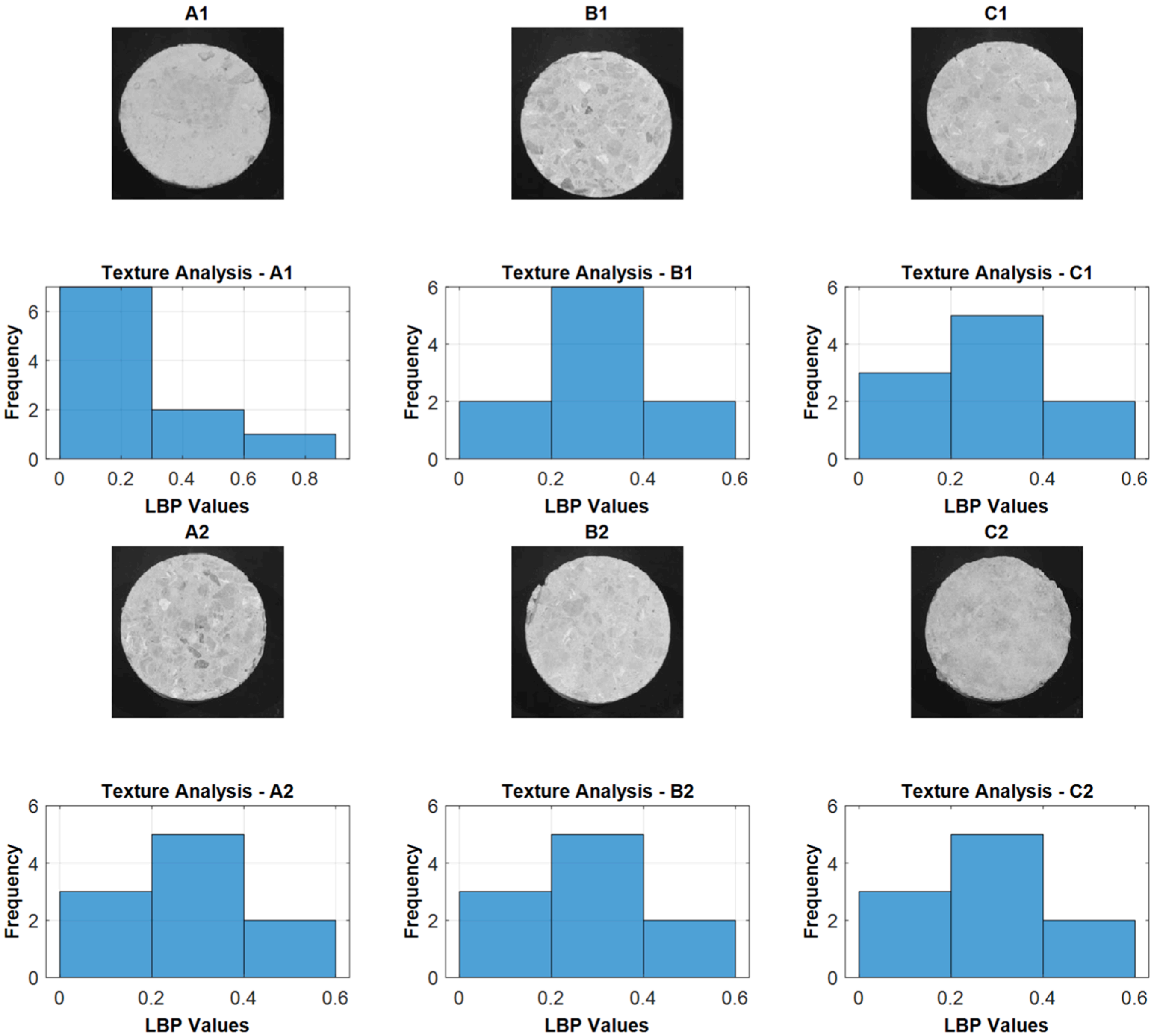

Fig. 7. LBP of horizontally cut concrete slices (A1, A2, B1, B2, C1, C2).

horizontal and vertical cuts of the concrete samples. LBP is a powerful image processing technique that captures the texture characteristics of an image by encoding the spatial structure of pixel intensities. Specifically, it analyzes a pixel's relationship with its surrounding neighbors and assigns a binary value based on whether the neighboring pixel intensities are higher or lower than the central pixel. The resulting LBP values provide a compact and informative representation of the image's texture. In the context of this study, LBP highlights the distribution and uniformity of aggregates, voids, and other features within the concrete. By offering detailed insights into the microstructural patterns of the samples, LBP enables a nuanced analysis that goes beyond conventional histogram-based approaches, making it particularly effective for identifying subtle texture variations in concrete surfaces.

Fig. 7 shows texture analyses for six concrete surface images, labeled A1, B1, C1, A2, B2, and C2, each accompanied by its Local Binary Pattern (LBP) frequency distribution histogram. In A1, the histogram shows that most LBP values are concentrated below 0.4, with a strong peak between 0.1 and 0.3, indicating a smoother and more uniform surface texture. In contrast, B1 exhibits a relatively balanced distribution across 0.1–0.5, with the highest frequency between 0.2 and 0.4, suggesting a rougher surface with greater textural complexity. Similarly, C1 displays a distribution centered around 0.2–0.4, though slightly more skewed towards lower LBP values than B1. For A2, most LBP values again fall below 0.4, but with a more even spread than A1, pointing to a moderately smooth surface. B2's histogram closely mirrors that of B1, with the highest frequencies around 0.2–0.4, reinforcing the observation of a rough texture. Lastly, C2 peaks in the 0.2–0.4 range but maintains a lower frequency at higher LBP values, suggesting a texture somewhat smoother than B2 but rougher than A1. Overall, the histograms reveal that A1 has the smoothest texture, while B1 and B2 have rougher and more varied textures, with C1 and C2 exhibiting intermediate characteristics.

Similarly, Fig. 8 illustrates the texture analyses of six concrete surface images labeled Ai, Aii, Bi, Bii, Ci, and Cii, each accompanied by its corresponding LBP frequency distribution histogram. In all six cases, the LBP values are predominantly concentrated in the lower range, particularly between 0 and 0.4. For Ai and Aii, the histograms show a strong peak between 0 and 0.2, with a gradual decline towards higher values,

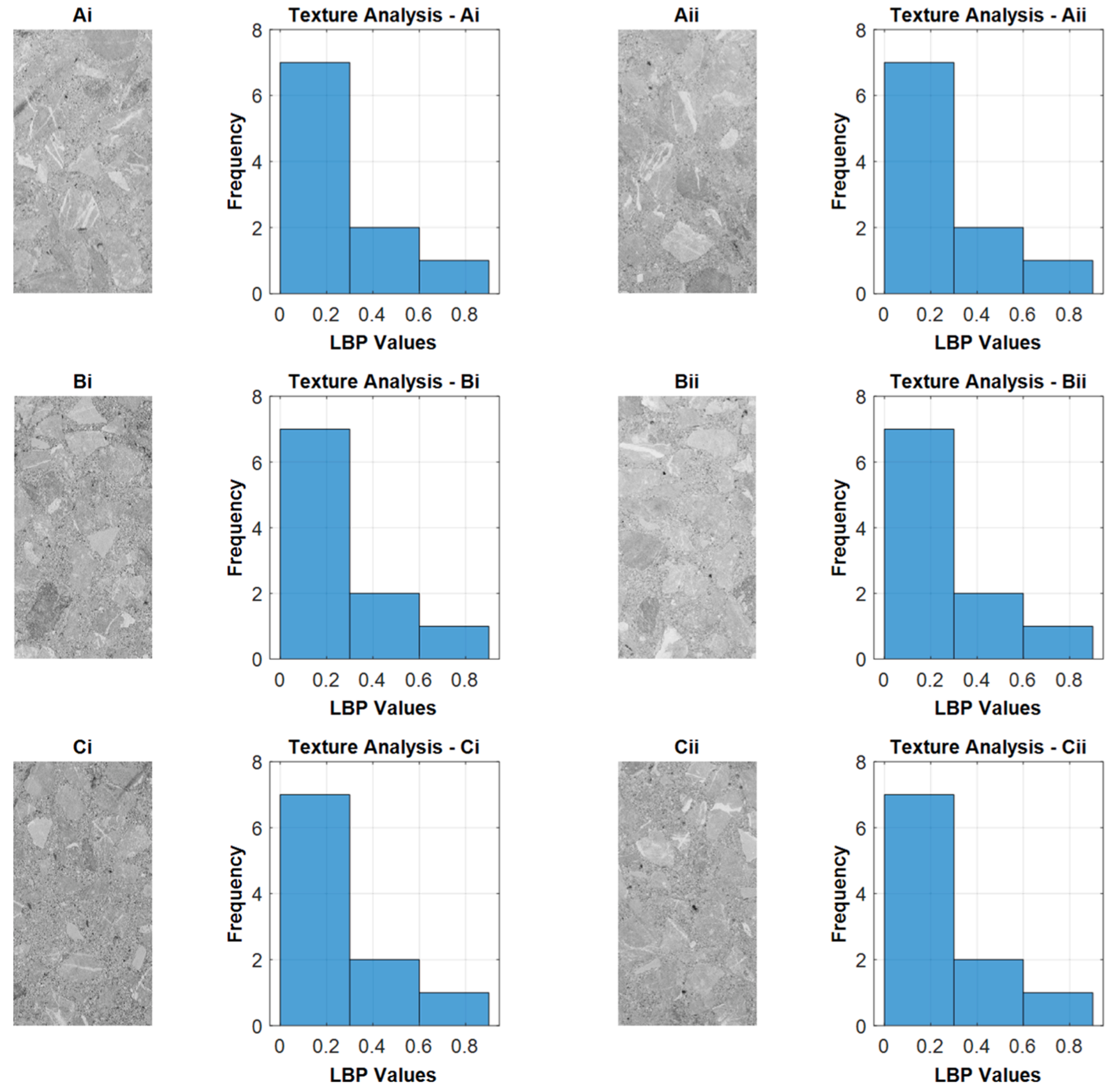

Fig. 8. LBP of vertically cut concrete slices (Ai, Aii, Bi, Bii, Ci, Cii).

and only a few frequencies observed beyond 0.6, suggesting a smooth and relatively uniform texture. Similarly, Bi and Bii demonstrate high frequencies at LBP values between 0 and 0.2, with fewer occurrences between 0.2 and 0.4, and minimal frequencies beyond 0.6, indicating comparable smoothness but slightly more textural variation than A samples. The Ci and Cii samples also show the highest frequencies in the 0–0.2 range, with a quick drop-off beyond 0.4, again suggesting surfaces that are largely uniform but potentially have finer texture differences than the A and B samples. Overall, across all samples, the dominant presence of low LBP values (especially below 0.4) reflects the generally smooth nature of the concrete surfaces, with minor variations between groups.

Fig. 9 presents the LBP histograms for the top faces of concrete specimens with a fixed mix ratio of 1:3:6, varying across different W/C ratios (0.4, 0.5, and 0.6) and CRM contents (0 %, 15 %, and 25 %). Each subplot includes a grayscale image of the concrete surface along with its corresponding LBP histogram, which quantifies texture distribution across the surface.

The figure demonstrates how both W/C ratio and CRM content influence the surface texture of the concrete, as reflected in the LBP value distributions. For instance, mixes with higher CRM percentages generally show narrower and more concentrated LBP distributions, indicating smoother and more uniform surface textures. This trend is particularly evident in the 0.4 and 0.5 W/C ratio rows, where the peak of the LBP histogram becomes sharper and shifts leftward as CRM content increases from 0 % to 25 %.

These textural changes correspond to the microstructural refinement induced by the pozzolanic activity of silica fume and fly ash, which fill voids and create a denser matrix. Additionally, variations in W/C ratio affect the moisture content and pore structure, which are also captured

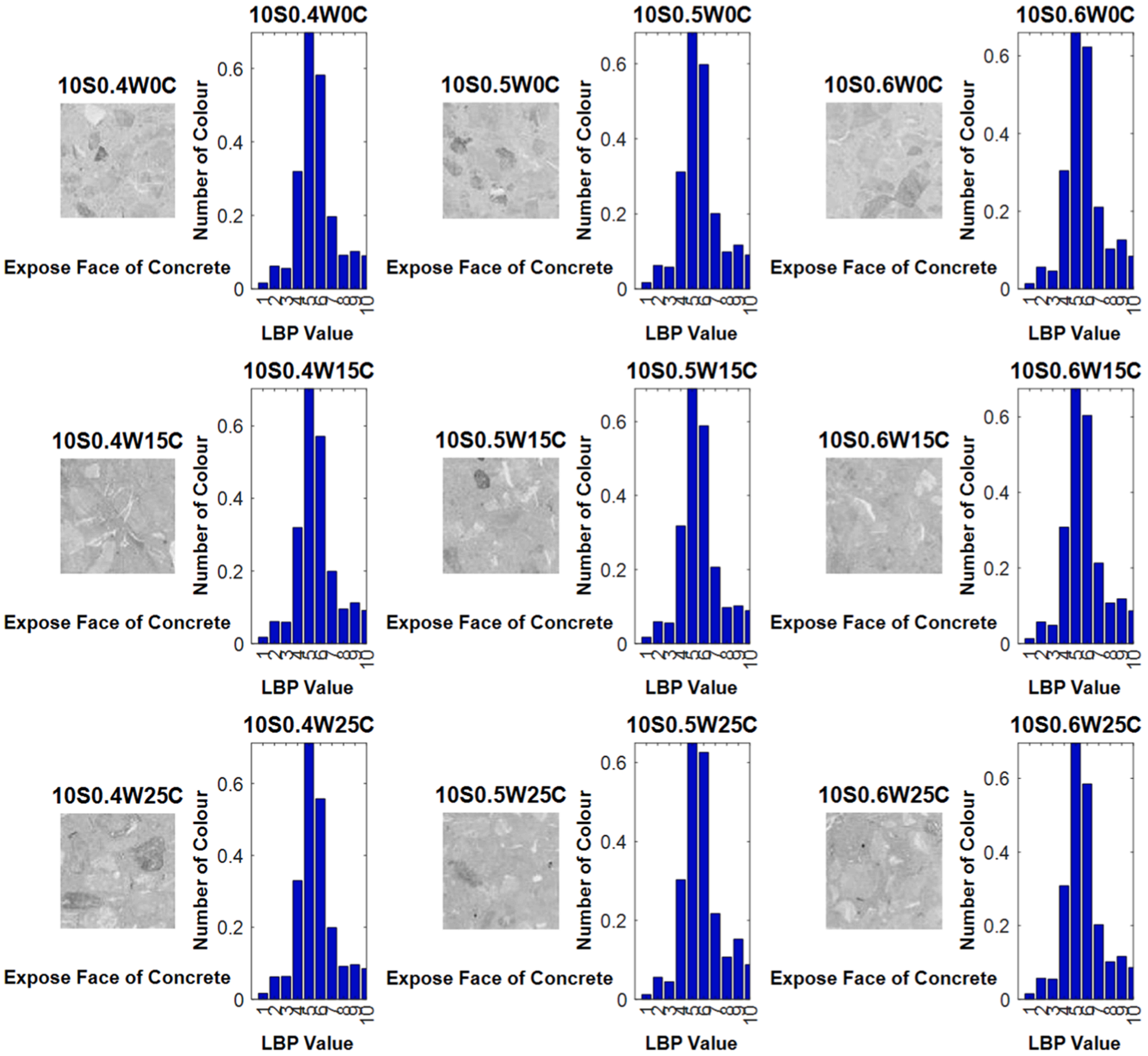

Fig. 9. LBP of 10S mix ratio at different W/C ratio and CRM.

by differences in the LBP histograms. The figure supports the observation that image-based texture features are sensitive to material composition and can be effectively used to infer properties such as f_c, thereby reinforcing the potential of the proposed image processing approach for nondestructive concrete evaluation.

Additionally, the impact of FA and SF on air voids within the concrete highlights how these additives alter the microstructure, thereby enhancing the material's overall durability.

Edge detection using the Canny method was employed to identify key features of the concrete specimens, such as aggregates, air gaps, and other structural components visible on the cut surfaces. This algorithm calculates intensity gradients within the images, effectively capturing only significant transitions while filtering out noise. The processing delineated two primary regions: (i) the edges outlining concrete boundaries and (ii) areas deemed non-relevant, which were excluded. Fig. 10 illustrates the original image alongside its edge-detected counterpart, showcasing the effectiveness of this method in isolating critical structural details.

The Canny edge detection algorithm operates through a series of precise steps: noise reduction using a Gaussian filter to smooth the image, calculation of intensity gradients to detect areas of rapid pixel value change, non-maximum suppression to refine and retain only sharp edges, and edge tracking through hysteresis to ensure reliable detection. Unlike masking, which simplifies the image into binary regions, the Canny method preserves intricate details, such as the outlines of aggregates and fine cracks, providing a more comprehensive representation of the concrete's texture. Its ability to adapt to varying lighting and texture conditions makes it superior to traditional binary thresholding, ensuring robustness even in challenging imaging scenarios. This enhanced detail and adaptability significantly improve the accuracy of subsequent analyses.

4. Prediction methodology

The statistical feature matrices extracted from concrete images, along with physical testing data containing f_c and f_t values obtained in

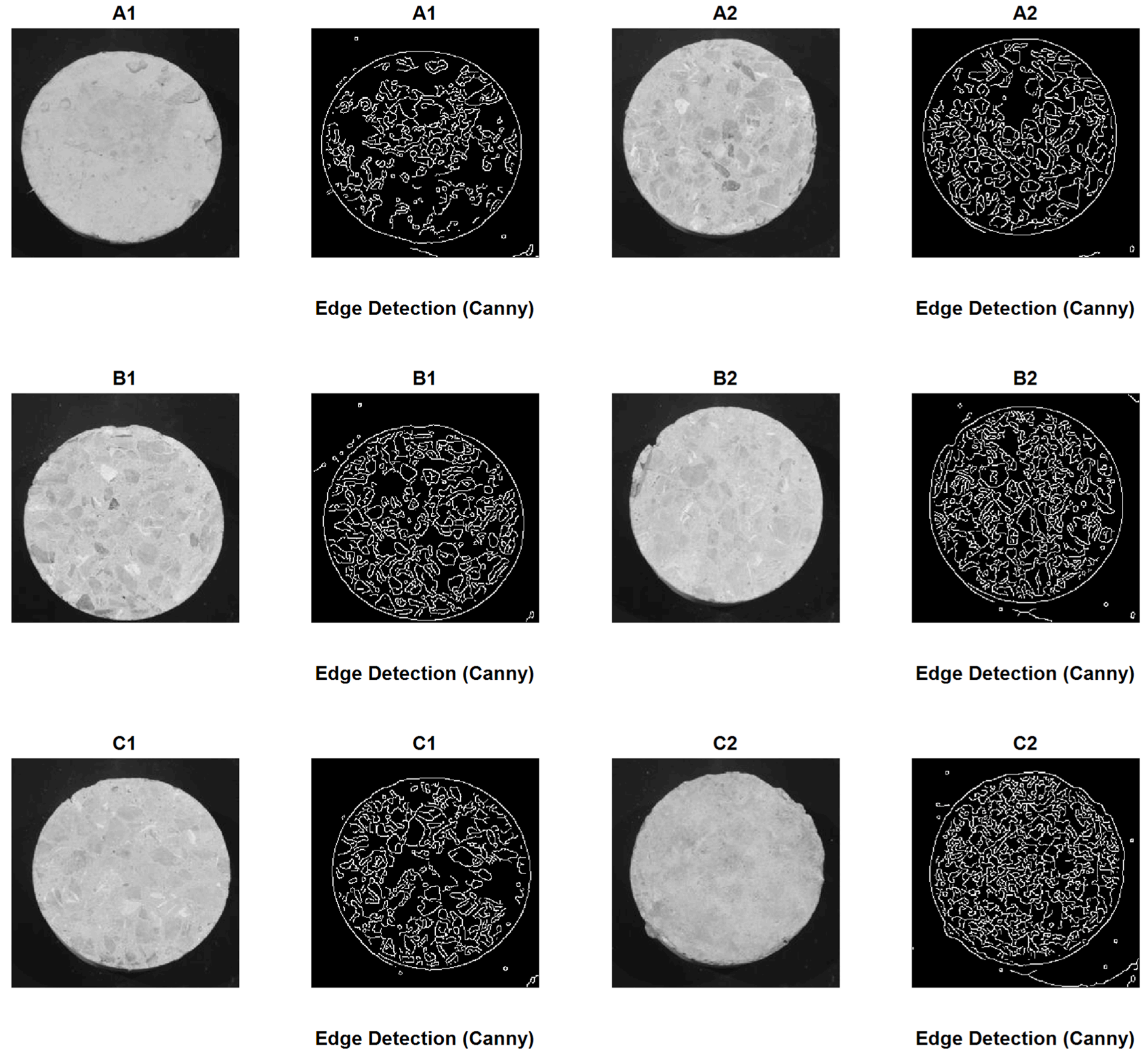

Fig. 10. Edge detection using the canny.

Section 3, were used as input and output data for the ML models. These models were developed to predict the mechanical properties of concrete based on image-derived features. This section provides details on building the ML models—SVM, BRE, and GPR—and explains how the dataset was utilized in the prediction process.

4.1. Support vector machine (SVM) model

SVM was introduced by Vapnik [66] to address high-dimensional problems. SVM is applicable to both regression and classification tasks [55]. In this study, SVM was utilized as a nonlinear regression model to predict the f_c and f_t values of hybrid concrete based on statistical features extracted from images. These statistical features served as predictors, while the laboratory-measured f_c and f_t values were the response variables in the SVM model.

For the developed dataset, the SVM regression function is mathematically expressed as Eq. (8):

$$f(a) = w \cdot \Phi(a) + b \tag{8}$$

where w represents weight vector, $\Phi(a)$ is the mapping function, and b denotes the bias. The Flatness of $f(a)$ is the Euclidean norm of the weight vector $\| w\|^2$, which should be minimized. For $f(a_i)$ to be optimal, the deviation between $f(a_i)$ and y_i must be smaller than ε. The insensitive factor (ε) measures the acceptable deviation level, and the deviation is computed using the following loss function and expressed as Eq. (9):

$$L_\varepsilon = \begin{cases} 0, & |y_i - f(a_i)| < \varepsilon \\ |y_i - f(a_i)| - \varepsilon_i, & |y_i - f(a_i)| \geq \varepsilon \end{cases} \tag{9}$$

In this loss function, $f(a)$ is influenced only by training points outside the ε-region, termed support vectors, while points inside the ε-region do not contribute to the optimization process. This issue is addressed using structural risk minimization, expressed as Eq. (10) [29]:

$$\min_{w,b,\xi_i,\xi_i^*} Q(w) = \frac{1}{2}\parallel w\|^2 + C\sum_{i=1}^{k}\left(\xi_i + \xi_i^*\right) \tag{10}$$

where ξ_i and ξ_i^* are slack variables to handle infeasible constraints, and C is a penalty term compensating for points within the ε-region. To minimize the loss, the following constraints apply and expressed as Eq. (11):

$$\begin{cases} y_i - w\cdot\Phi(a) - b \ \leq\ \varepsilon + \xi_i \\ w\cdot\Phi(a) + b - y_i \ \leq\ \varepsilon + \xi_i^* \\ \xi_i = 0 \\ \xi_i^* = 0 \end{cases} \tag{11}$$

Lagrange multipliers ($e_i, e_j^*, \mu_i, \mu_i^*$) are introduced in Eq. (12) and Eq. (13), to solve the problem. The multipliers should be non-negative, and the resulting equation of loss function is given as Eq. (14). However, Lagrange multipliers can be applied in conjunction with Karush-Kuhn-Tucker (KKT) complimentary conditions (cc) given in Eq. (15) to achieve optimum SVM function [29,55]. The weight vector w for the regression is determined through solving the expression $w = \sum_{i=1}^{k}\left(e_i - e_i^*\right)\Phi(a_i)$.

$$\begin{aligned} L_{\varepsilon,w,b,e,\mu} = \frac{1}{2} \\ \parallel w\|^2 + C\sum_{i=1}^{k}\left(\xi_i + \xi_i^*\right) - \varepsilon\sum_{i=1}^{k}\left(e_i(\varepsilon + \xi_i - y_i + w\cdot\Phi(a_i) + b)\right) \\ - \sum_{i=1}^{k}\left(e_j^*(\varepsilon + \xi_i - y_i + w\cdot\Phi(a_i) - b)\right) - \sum_{j=1}^{k}(\mu_i\xi_i + \mu_i^*\xi_i^*) \end{aligned} \tag{12}$$

$$cc = \begin{cases} e_i(\varepsilon + \xi_i - y_i + w\cdot\Phi(a) + b\,) = 0 \\ e_i^*(\varepsilon + \xi_i + y_i - w\cdot\Phi(a) - b\,) = 0 \\ (C - e_i)\xi_i = 0 \\ \left(C - e_i^*\right)\xi_i^* = 0 \end{cases} \tag{13}$$

$$\begin{aligned} L_a = \frac{1}{2}\sum_{i=2}^{k}\sum_{j=1}^{k}\Bigg(\left(e_i - e_i^*\right)\left(e_j - e_j^*\right)a_i^T a_j - \varepsilon\sum_{i=1}^{k}\left(e_i - e_i^*\right) + \sum_{j=1}^{k} y_i\Big(e_j \\ - e_j^*\Big)\Bigg) \end{aligned} \tag{14}$$

$$\begin{cases} \sum_{i=1}^{k}\left(e_i - e_i^*\right) = 0 \\ 0 \leq e_i \leq C \\ 0 \leq e_i^* \leq C \end{cases} \tag{15}$$

Eq. (16) represents the SVM regression function without incorporating a kernel function. Based on recommendations from previous studies [67,68], the RBF kernel is employed in this study. The performance of the SVM model with the RBF kernel is primarily influenced by sample variance and regularization. The mathematical expression for the RBF kernel is provided in Eq. (17) and Eq. (18) which represents the SVM regression function with the RBF kernel.

$$f(a) = \sum_{i=1}^{k}\left(e_i - e_i^*\right)\cdot\Phi(a_i)\cdot a + b \tag{16}$$

$$G(a_i, a_j) = \exp\left(-||a_i - a_j||^2 \big/ \sigma^2\right) \tag{17}$$

$$f(a) = \sum_{i=1}^{k}\left(e_i - e_i^*\right)G(a_i, a_j) + b \tag{18}$$

Eq. (18) represents the nonlinear regression function of SVM used in this study to predict the mechanical properties of HC based on image features. The model's estimation performance can be evaluated using appropriate performance indicators.

4.2. Boosted ensemble regression (BRE) model

Ensemble regression combines multiple supervised learning models to improve the accuracy of predictions compared to a single base model. The individual models within the ensemble are referred to as base learners. Ensemble methods leverage the information gained from each weak learner, adjusting bias and variance to enhance the performance and reliability of the final response value [69].

Two commonly used ensemble techniques are boosting [70] and bagging [71]. Bagging is a parallel approach that is particularly effective for high-variance estimations. In bagging, base learners are trained independently on subsets of the training data, and their predictions are averaged to produce the final output. Boosting, in contrast, is a sequential technique designed to address high bias and variance in estimations. In boosting, new learners are built sequentially, using the data and errors from previous weak learners. This process places greater emphasis on data points with higher inaccuracies in each iteration, increasing the estimation power of the model [72].

Through multiple cycles, the weak learners are iteratively refined, and their predictions are combined to construct a robust and reliable predictive model [30,55]. The mathematical formulation of ensemble algorithms is provided in Eq. (19).

$$f(a) = z_k - \eta f(a_k) \tag{19}$$

In this context, $f(a)$ represents the new learner, k denotes the sample number in the dataset, z_k is the ground truth, $f(a_k)$ represents the cumulative prediction of the previous weak learner, and η is the learning rate. Boosting algorithms introduced by Friedman [71], such as LSBoost, MBoost, and LADBoost, utilize different loss functions. For instance, LSBoost employs the least squares loss function, MBoost uses the Huber loss, and LADBoost is based on the least absolute deviation. In this study, the LSBoost function was applied with ensemble algorithms to estimate the mechanical properties of HC using the generated dataset.

The implementation of the LSBoost algorithm for this problem as, the model is initially set to the average of the target values, denoted by $\bar{z}$, as Eq. (20).

$$f_0(a) = \bar{z} \tag{20}$$

For m iterations during modeling:

For $m = 1$, and for $i = 1$ to N (the number of datasets), pseudo-responses ($\check{z}$) are calculated using the target values (z_k) and the model's predicted values, as Eq. (21).

$$\check{z}_i = z_k - f_{n-1}(a_i) \tag{21}$$

The pseudo-responses ($\check{z}$) are optimized using the least squares function as follows, as Eq. (22).

$$(\alpha_m, b_m) = argmin_{b,\alpha}\sum_{i=1}^{N}\left[\check{z}_i - \alpha h(a_i; b)\right]^2 \tag{22}$$

Here, $h(a;b)$ represents the boosted weak model.

The generalized LSBoost ensemble regression algorithm for m iterations is formalized in Eq. (20) and as expressed as Eq. (23)

$$f_m(a) = f_{m-1}(a) + a_m h(a; b_m) \tag{23}$$

Key parameters influencing the prediction performance of the boosting algorithm are the number of trees and the learning rate [69, 72]. To avoid overfitting during training, researchers [73] recommend selecting a low learning rate.

4.3. Gaussian process regression (GPR) model

GPR is a nonparametric probabilistic supervised learning technique within ML, known for its ability to capture complex relationships between predictors and responses with high accuracy [58]. GPR is applicable to both regression and classification tasks. It defines a probabilistic distribution over a latent function to interpolate observations, allowing the deviation of Gaussian probability from actual values to be computed [69]. This deviation helps GPR identify the necessary refinements in regions of interest, making it an efficient tool for regression problems [47].

The performance of a GPR model can be enhanced through the use of kernel functions. In this study, kernel-based GPR is applied as a nonlinear regression tool to predict the mechanical properties of HC. The squared exponential kernel, expressed in Eqs. 20 and 21 [47,69], is used in the GPR model.

For the dataset $D = (a_{i,}z_i)$, where a_i represents the statistical image features matrix of size $m \times n$, and z_i is the laboratory values vector of size $m \times 1$, the GP function is defined in Eq. (24).

$$f(a) = GP(m(a), k(a, a')) \tag{24}$$

Where $m(a)$ is mean function and $k(a, a')$ represents the covariance function as Eq. (25).

$$k(a, a') = \sigma_f^2 \exp\left(-\frac{||\alpha - \alpha'||^2}{2l^2}\right) + \sigma_n^2 \delta(\alpha, \alpha') \tag{25}$$

Where σ_f^2 is the maximum acceptable variance for the function, l is the length parameter, $\delta(a, a')$ denotes Kronecker delta function. Noisy output (O) of the GPR model can be computed through function ($f(a)$) with Gaussian noise $\mathscr{L}$ of the model for n observations subjected to normal distribution [d(0, σ^2)] with mean $= 0$ and variance $= \sigma^2$ as expressed in Eq. (26).

$$O_i = f(a_i) + \mathscr{L} \tag{26}$$

Covariance is the significant parameter of GPR, it calculates the effect of outputs with each other. To achieve ultimate performance, it is recommended to compute the following three covariance matrices for the previous input vector (a) and new input vector (a_*), as discussed in Eqs. (27)-(29).

$$K = \begin{bmatrix} k(a_1, a_1) & k(a_1, a_2) & \ldots\ldots & k(a_1, a_n) \\ k(a_2, a_1) & k(a_2, a_2) & \ldots\ldots & k(a_2, a_n) \\ \vdots & \vdots & & \vdots \\ k(a_n, a_1) & k(a_n, a_2) & \ldots\ldots & k(a_n, a_n) \end{bmatrix} \tag{27}$$

$$K_* = [\, k(a_*, a_1) \quad k(a_*, a_1) \quad k(a_*, a_1) \,] \tag{28}$$

$$K_{**} = k(a_*, a_*) \tag{29}$$

The probability density function as discussed in Eqs. (30)-(32).

$$p(O^*|t) = d(\text{mean}, \text{Var}) \tag{30}$$

$$\text{Mean}(O_*) = K_* K^{-1} O \tag{31}$$

$$\text{Var}(O_*) = K_{**} - K_* K^{-1} K_*^T \tag{32}$$

Based on the above mathematical formulations, the estimated value of the GPR model corresponds to the mean of the distribution, while the variance of the distribution quantifies the uncertainty. The model parameters, σ_n and k, are determined using Bayesian theory by specifying the hyperparameters of the GPR function [47,58].

5. Results and discussions

5.1. Effect of CRM on mechanical characteristics

In this section we examine the laboratory test results and in particular how the presence of CRMs affects the mechanical characteristics of hybrid concrete, in terms of f_c and f_t. Several factors influence the mechanical characteristics of concrete, including the W/C ratio, curing conditions, the presence of CRMs, cement content, compaction method, aggregate size, and specimen shape. FA and SF, as CRMs, exhibit pozzolanic activity, enhancing the formation of calcium silicate hydrate and improving the strength of HC. FA's pozzolanic reaction is slower, contributing to increased compressive strength at later ages, while SF demonstrates PA at earlier stages [10,15,16]. The results for the compressive strength are presented in Fig. 11 for the 14-days and the 28-days curing period.

Initially, concrete containing SF and FA shows relatively low compressive strength, but this strength increases significantly with time, particularly at 28 days, as illustrated in Fig. 11. For instance, at 14 days, a specimen with 0 % SF and FA (blue bar) and a W/C ratio of 0.4 (i.e. case 5.5S0.4W14D) achieves the maximum f_c of approximately 16 MPa, whereas a similar specimen containing 25 % SF and FA reaches 24 MPa (green bar for the same case). This trend remains consistent across other mix ratios, highlighting the beneficial impact of CRMs on the mechanical properties of concrete. FA exhibits a delayed pozzolanic reaction, while SF initiates its PA earlier, contributing to the gradual increase in compressive strength at later ages [10,15,16].

The results for f_t are presented in Fig. 12 following a similar pattern. The data indicates that cylindrical samples without CRM (0 % replacement) exhibit significantly lower f_t compared to those incorporating CRM. This improvement in f_t is attributed to the enhanced interfacial bond within the concrete matrix, achieved by replacing cement with finer materials like SF and FA [10,15,16]. The finer particle size of SF and FA, relative to traditional cement, results in denser packing and improved adhesion between the cement paste and aggregates, thereby enhancing the tensile properties of the modified concrete in all examined cases.

In general, the results indicate that incorporating SF and FA positively impacts the strength of HC. HC specimens containing 25 % CRM (SF and FA) demonstrated superior strength compared to those with 15 % or 0 % CRM. This enhancement in strength is attributed to the increased pozzolanic effect provided by the presence of SF and FA.

5.2. Analysis of models' performance

To ensure accuracy, predictive models must be validated using appropriate techniques. Two common validation methods are (i) single validation and (ii) k-fold cross-validation [28]. In the single validation method, the dataset is randomly split into training and testing sets. The training set is used to build strong learners from weak base models, while the testing set evaluates the model's prediction accuracy. Typically, the dataset is divided in an 80/20 ratio, with 80 % for training and 20 % for testing, though other ratios such as 70/30 or 90/10 can also be used [20].

The k-fold cross-validation method, based on the Jackknife test, reduces data bias by randomly dividing the dataset into k equal subsets. The model is trained using (k-1) subsets, while the remaining subset is used for validation. This process is repeated k times, and the average accuracy of all iterations is calculated. A 10-fold cross-validation is often preferred for ensuring generalization and reliability of model performance [46].

In this study, both 10-fold cross-validation and the 80/20 single-validation method were applied. Additionally, the model's performance was assessed using five performance indicators: Pearson's correlation coefficient (R), coefficient of determination (R^2), mean absolute error (MAE), mean absolute percentage error (MAPE), mean squared

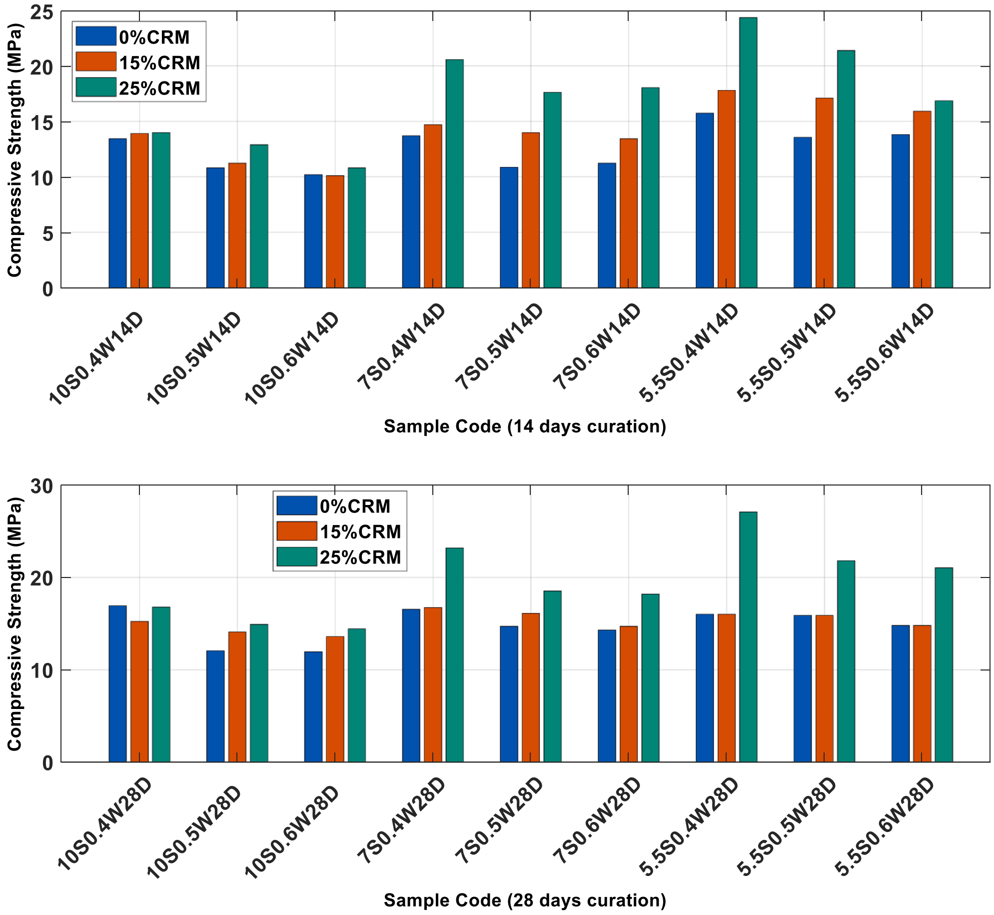

Fig. 11. Laboratory obtained values of compressive strength f_c of hybrid concrete for different percentages of *CRM*.

error (MSE), and root mean square error (RMSE). A detailed investigation of performance metrics in regression analysis and ML-based prediction models can be found in [74]. The mathematical definitions of these indicators are provided in Eqs. (33)-(38), where P represents the predicted (estimated) value, T represents the target values, $\overline{P}$ is the mean predicted value, and $\overline{\mathrm{T}}$ is the mean target value.

$$R = \frac{\sum_{i=1}^{n}(P_i - \overline{P})(T_i - \overline{T})}{\sqrt{\sum_{i=1}^{n}(P_i - \overline{P})^2 \cdot \sum_{i=1}^{n}(T_i - \overline{T})^2}} \tag{33}$$

$$R^2 = 1 - \frac{\sum_{i=1}^{n}(P_i - T_i)^2}{\sum_{i=1}^{n}(T_i - \overline{T})^2} \tag{34}$$

$$MAE = \frac{1}{n}\sum_{i=1}^{n}|P_i - T_i| \tag{35}$$

$$\mathrm{MAPE} = 100 \cdot \frac{1}{n}\sum_{i=1}^{n}\left|\frac{P_i - T_i}{T_i}\right| \tag{36}$$

$$\mathrm{MSE} = \frac{1}{n}\sum_{i=1}^{n}(P_i - T_i)^2 \tag{37}$$

$$\mathrm{RMSE} = \sqrt{\frac{1}{n}\sum_{i=1}^{n}(P_i - T_i)^2} \tag{38}$$

The performance of three ML models integrated with IP for predicting f_c and f_t was evaluated using single validation and is summarized in Table 4. The statistical parameters demonstrate the models' predictive capabilities based on data extracted through IP. The results reveal that the models exhibited high precision and flexibility in handling unseen data.

The IP-SVM model demonstrated superior performance with R^2 values of 0.965 for f_c and 0.947 for f_t, as shown in Fig. 13 and Fig. 16. Compared to the model performance of the IP-BRE model, with an R^2 value of 0.918 and 0.915 for f_c and f_t, respectively, as depicted in Fig. 15 and Fig. 16, and the model performance of IP-GPR with an R^2 value of 0.939 for predicting f_c, as shown in Fig. 15 and 0.948 for predicting f_t, as illustrated in Fig. 18. Other statistical performance indicators, including Pearson's correlation coefficient (R), mean squared error (MSE), root mean square error (RMSE), mean absolute error (MAE), and mean absolute percentage error (MAPE), further validated the model' performance. For the IP-SVM model, the values for f_c were $R = 0.999$, MSE $= 0.0120$, RMSE $= 0.117$, MAE $= 0.0070$, and MAPE $= 0.701$. For f_t, the values were: $R = 0.999$, MSE $= 0.00076$, RMSE $= 0.0242$, MAE $= 0.0060$, and MAPE $= 0.602$. The models were also validated using 10-fold cross-validation, with results shown in Table 5. The fluctuations between single validation and 10-fold cross-validation models ranged from 0.02 % to 0.05 %, confirming the robustness of the models.

The prediction performance comparison between IP-SVM, IP-BRE and IP-GPR reveals that IP-GPR consistently offers superior generalization, particularly for f_c. In both single validation and 10-fold cross-validation, IP-GPR achieved the lowest values for MSE, RMSE, MAE, and MAPE error metrics, indicating more accurate and stable f_c predictions, despite having slightly lower R^2 values than IP-SVM. For f_t, IP-SVM performed competitively and even slightly outperformed IP-GPR in

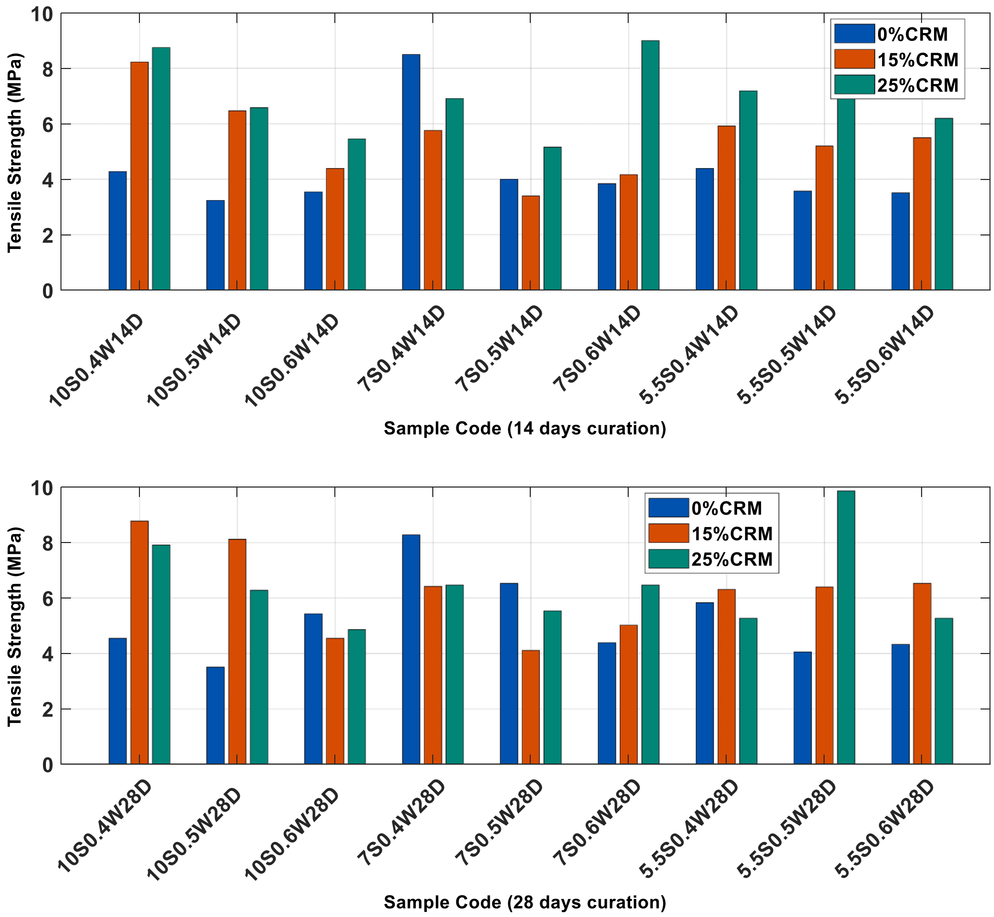

Fig. 12. Laboratory obtained values of split-tensile strength f_t of hybrid concrete for different percentages of CRM.

Table 4
Prediction performance of the ML models (single validation).

	R	R^2	*MSE*	*RMSE*	*MAE*	*MAPE*
f_c						
Training data						
IP-SVM	0.999	0.999	0.000310	0.0180	0.0008	0.081
IP-BRE	0.999	0.999	0.000352	0.0189	0.0007	0.078
IP-GPR	0.990	0.999	0.000348	0.0189	0.0007	0.076
Testing data						
IP-SVM	0.999	**0.965**	0.01200	0.1170	0.0070	0.701
IP-BRE	0.999	0.918	0.01120	0.1059	0.0066	0.664
IP-GPR	0.999	0.939	**0.00870**	**0.0930**	**0.0064**	**0.647**
f_t						
Training data						
IP-SVM	0.999	0.999	0.03130	0.1900	0.0250	2.526
IP-BRE	0.999	0.996	0.04330	0.2080	0.0350	3.526
IP-GPR	0.999	0.999	0.03350	0.0057	0.0007	0.071
Testing data						
IP-SVM	0.999	0.947	**0.00076**	**0.0242**	0.0060	0.602
IP-BRE	0.999	0.915	0.00239	0.0489	0.0097	0.978
IP-GPR	0.999	**0.948**	0.00079	0.0282	**0.0058**	**0.584**

some cases, such as RMSE and MAE during cross-validation. However, IP-GPR still maintained the lowest MAPE, reflecting better relative error performance. In contrast, IP-BRE underperformed across all metrics, demonstrating higher error values and lower R^2 in both validation approaches. Overall, while IP-SVM proves to be a strong method for predicting f_t, IP-GPR stands out as the most robust and reliable model across both f_c and f_t.

The models' ability to correlate pixel-level data from images with the mechanical properties of concrete is evident. Statistical features extracted from images enabled the models to establish strong associations between these features and concrete characteristics. These relationships were validated using test data processed through the models, confirming the models' reliability. This study highlights the potential of combining ML with IP to predict the mechanical properties of concrete, offering a promising approach for practical applications [40–42,55].

6. Conclusions

This study presented a nondestructive methodology for estimating the mechanical properties of hybrid concrete by integrating image processing and machine learning techniques. Statistical features were extracted from grayscale images of concrete specimens and used to train and evaluate three supervised ML models: IP-SVM, IP-BRE, and IP-GPR. The results demonstrate that integrating IP with ML offers a fast, nondestructive alternative to traditional concrete assessment methods. This approach enhances efficiency, reduces costs, and supports more sustainable practices in construction quality control and structural health monitoring.

The incorporation of CRMs, such as silica fume and fly ash, significantly enhanced the mechanical properties of HC. Specimens with higher CRM content consistently exhibited improved performance, highlighting the value of using sustainable materials in concrete production. This methodology aligns with the broader industry goal of developing environmentally friendly and cost-effective construction materials.

Despite the promising results, the study has some limitations. The models were developed using a relatively small dataset with fixed mix proportions and only two types of CRMs. As such, the findings may not fully generalize to broader applications involving diverse concrete

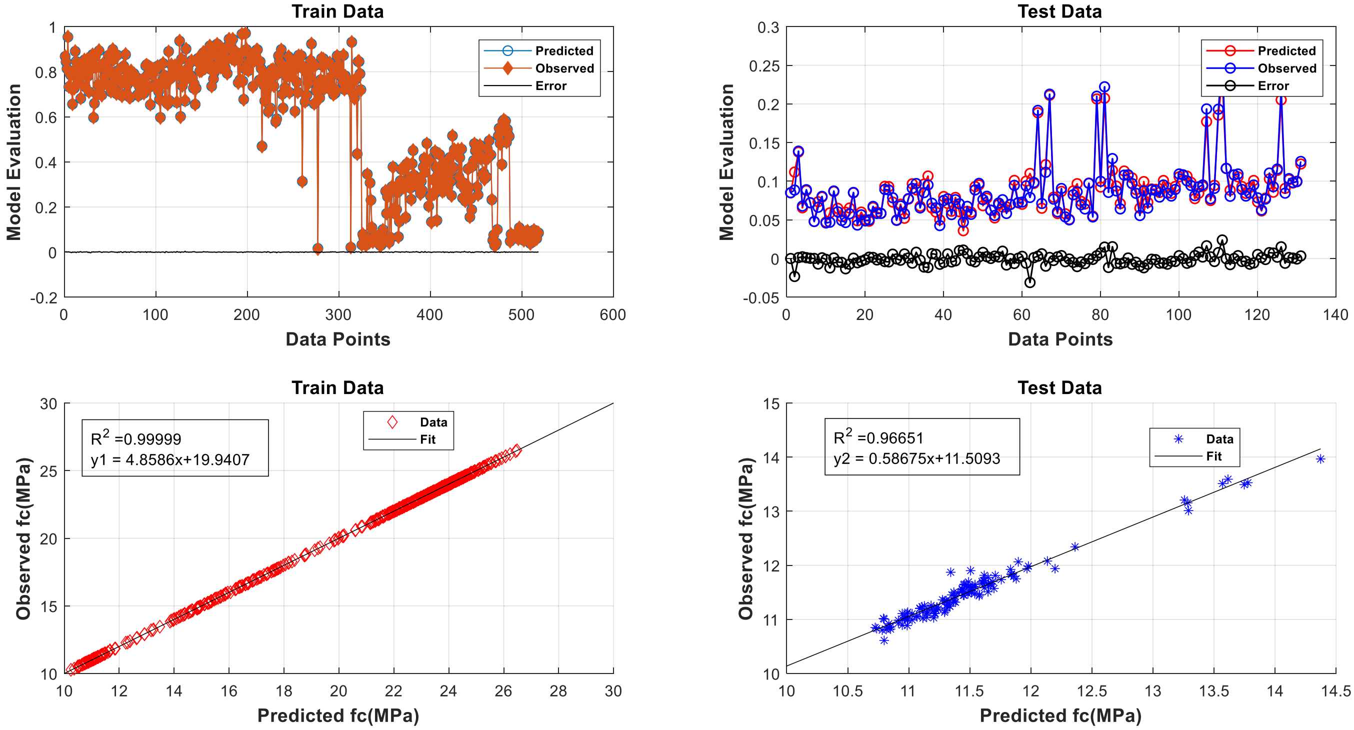

Fig. 13. Error distribution and observed vs predicted comparison of IP-SVM for f_c of concrete.

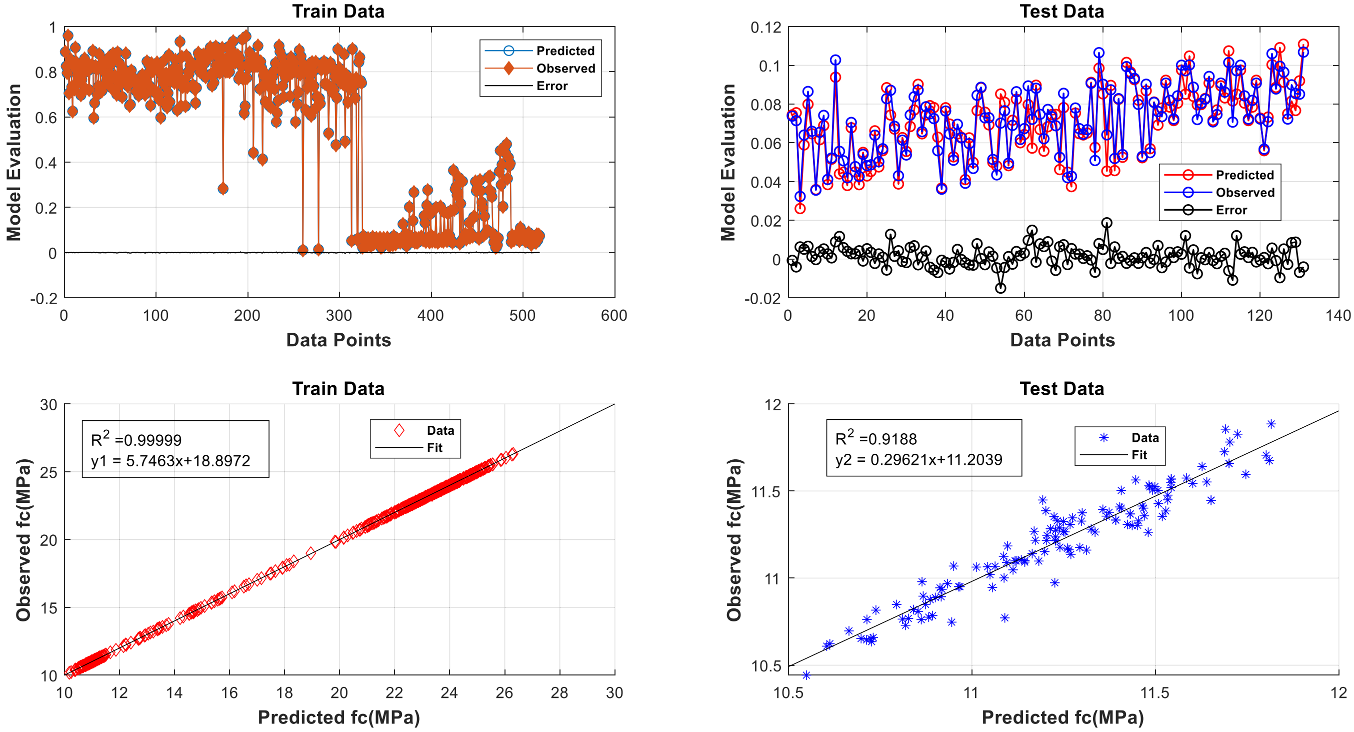

Fig. 14. Error distribution and observed vs predicted comparison of IP-BRE for f_c of concrete.

compositions or environmental conditions. Future research will aim to expand the dataset, incorporate a wider variety of CRMs, and explore the influence of different image resolutions and advanced image-based descriptors.

Overall, this research highlights the potential of IP-ML integration as a fast, cost-effective, and scalable tool for concrete quality assessment. With further validation, this methodology can support more efficient construction practices and improve SHM techniques. Beyond strength estimation, image processing techniques hold promise for detecting cracks, voids, and surface defects, as well as for estimating properties such as homogeneity and water-to-cement ratio—critical factors in evaluating concrete integrity.

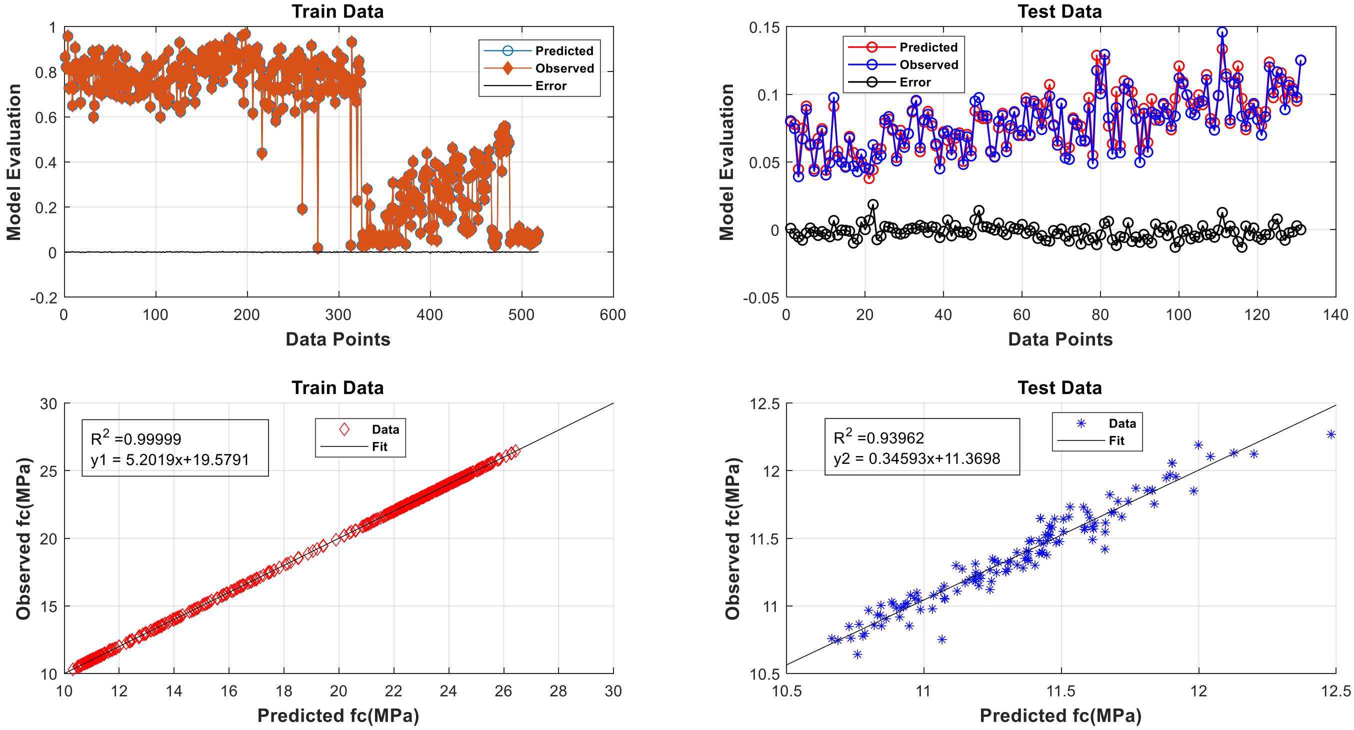

Fig. 15. Error distribution and observed vs predicted comparison of IP-GPR for f_c of concrete.

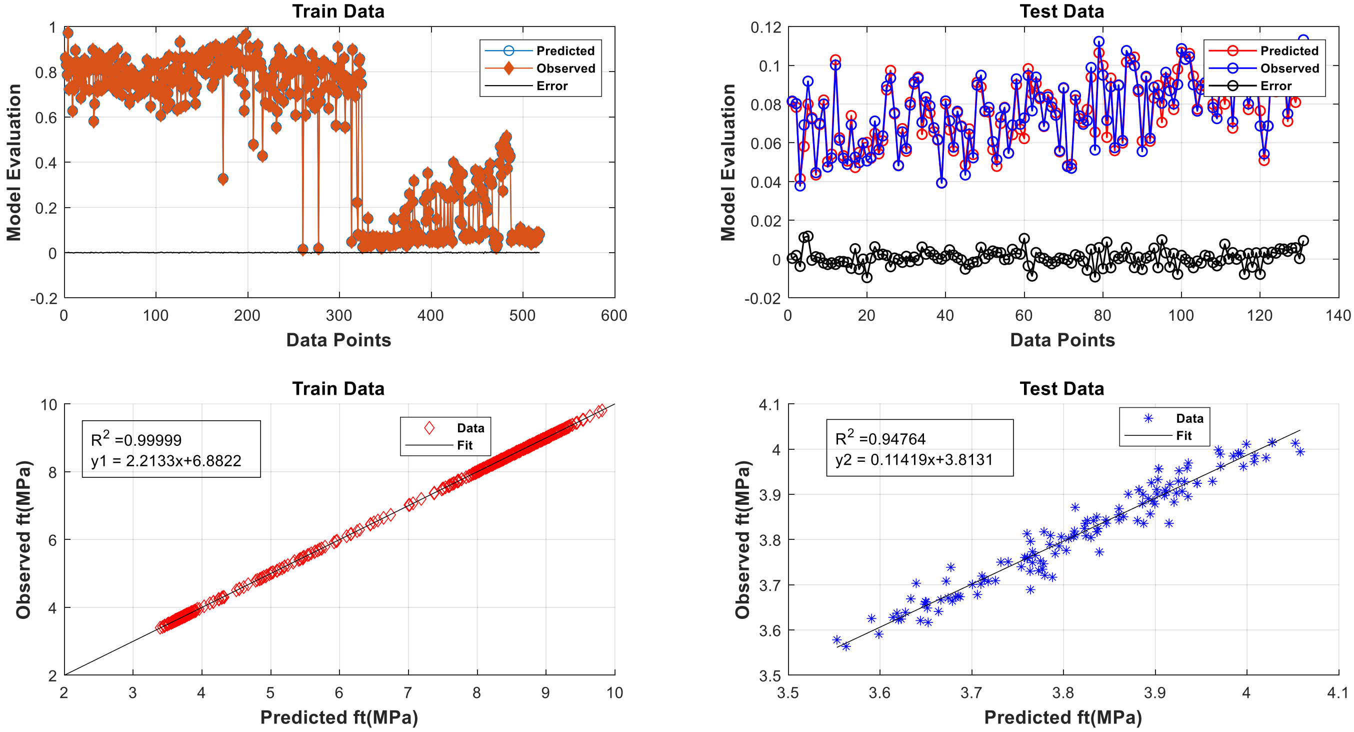

Fig. 16. Error distribution and observed vs predicted comparison of IP-SVM for f_t of concrete.

CRediT authorship contribution statement

Ammar T. Al-Sayegh: Writing – review & editing, Writing – original draft, Visualization, Supervision, Software, Investigation, Formal analysis, Data curation. **Vagelis Plevris:** Writing – review & editing, Writing – original draft, Visualization, Supervision, Software, Project administration, Methodology, Investigation, Formal analysis, Conceptualization. **Afaq Ahmad:** Writing – review & editing, Writing – original draft, Validation, Resources, Project administration, Methodology, Data curation, Conceptualization. **Junaid Mir:** Writing – review & editing, Validation, Resources, Methodology, Formal analysis, Conceptualization.

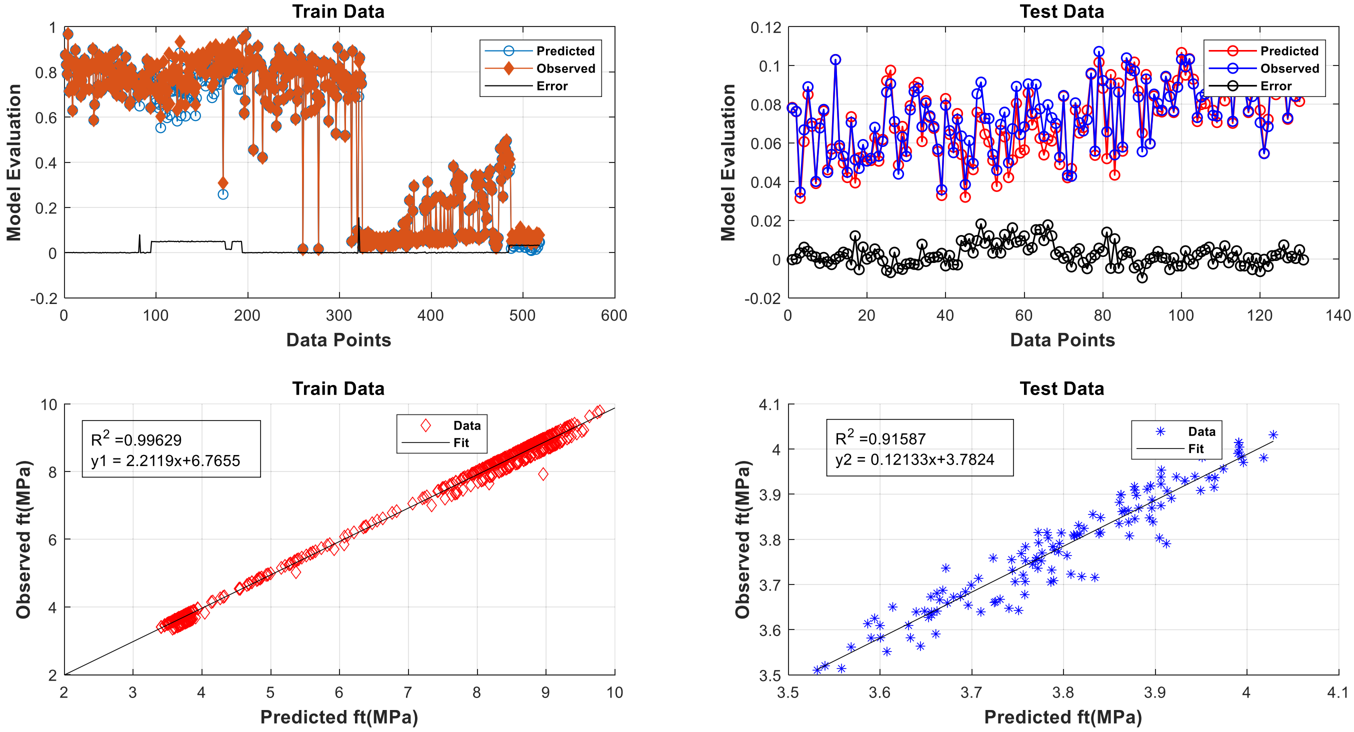

Fig. 17. Error distribution and observed vs predicted comparison of IP-BRE for f_t of concrete.

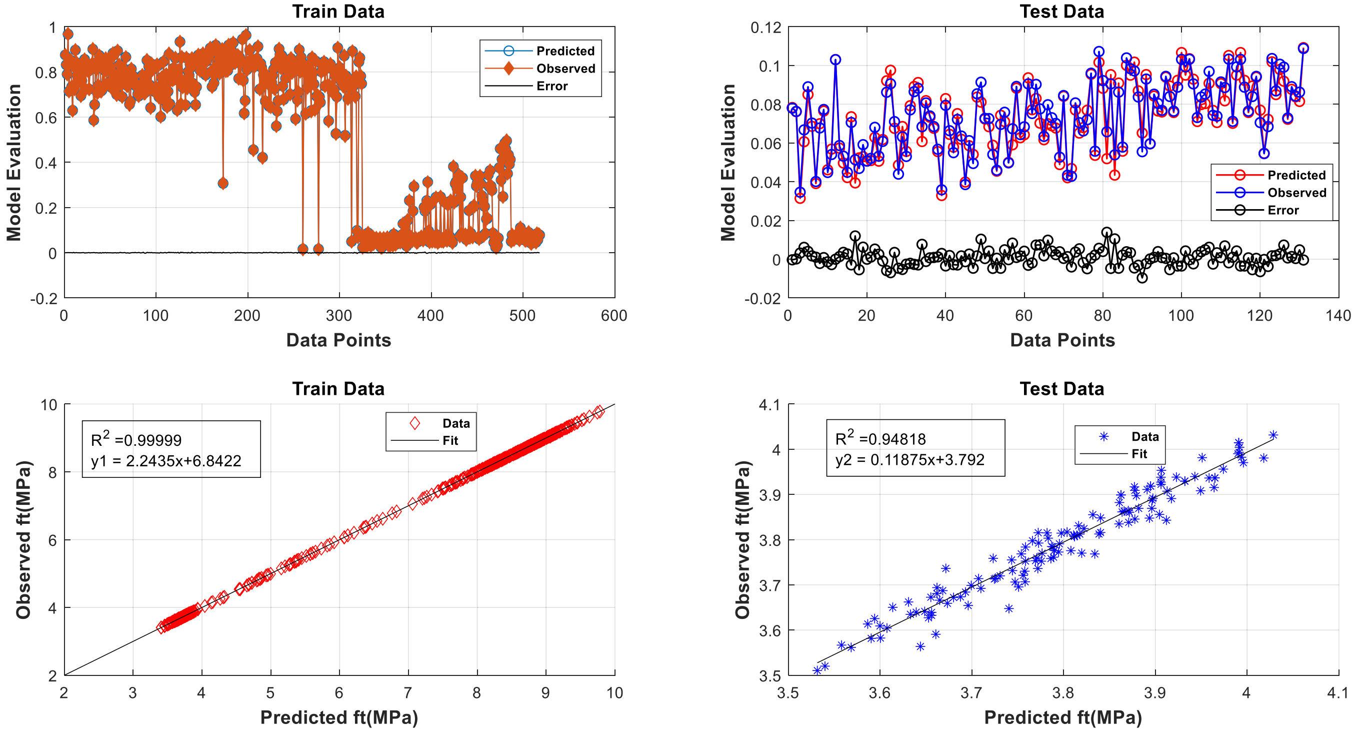

Fig. 18. Error distribution and observed vs predicted comparison of IP-GPR for f_t of concrete.

Ethics statement

This study does not involve human participants, animal subjects, or any experiments requiring ethical approval.

Informed consent and consent to publish

This study does not involve human participants, personal information, or identifiable data, such as names, photographs, or other distinguishing characteristics. Therefore, informed consent and consent to publish are not applicable and were not required for this research.

Table 5
Prediction performance of the ML models (10-fold cross validation).

		R	R^2	MSE	RMSE	MAE	MAPE
f_c							
	IP-SVM	0.99	**0.970**	0.01000	0.1170	0.0069	0.70
	IP-BRE	0.99	0.938	0.01020	0.1050	0.0054	0.55
	IP-GPR	0.99	0.957	**0.00767**	**0.0810**	**0.0040**	**0.47**
f_t							
	IP-SVM	0.99	**0.950**	0.00071	**0.0242**	**0.0058**	0.60
	IP-BRE	0.99	0.935	0.00290	0.0409	0.0087	0.90
	IP-GPR	0.99	0.943	**0.00070**	0.0250	0.0060	**0.58**

Funding

This project has received funding from the European Union's Horizon 2020 research and in-novation program under the Marie Sklodowska–Curie grant agreement No. 101153307 (https://cordis.europa.eu/project/id/101153307).

Declaration of Competing Interest

The authors declare that they have no known competing financial interests or personal relationships that could have appeared to influence the work reported in this paper.

Data availability

Data sets generated during the current study are available from the corresponding author on reasonable request.

References

[1] Dorafshan S, Thomas RJ, Maguire M. Benchmarking image processing algorithms for unmanned aerial system-assisted crack detection in concrete structures. Infrastructures 2019;4(2):19. https://doi.org/10.3390/infrastructures4020019.

[2] Flah M, Nunez I, Ben Chaabene W, Nehdi ML. Machine learning algorithms in civil structural health monitoring: a systematic review. Arch Comput Methods Eng 2021;28(4):2621–43. https://doi.org/10.1007/s11831-020-09471-9.

[3] Hu C, Li Z. Property investigation of individual phases in cementitious composites containing silica fume and Fly ash. Cem Concr Compos 2015;57:17–26. https://doi.org/10.1016/j.cemconcomp.2014.11.011.

[4] Plevris V, Papazafeiropoulos G. AI in structural health monitoring for infrastructure maintenance and safety. Infrastructures 2024;9(12). https://doi.org/10.3390/infrastructures9120225.

[5] Gallucci L, et al. An embedded wireless sensor network with wireless power transmission capability for the structural health monitoring of reinforced concrete structures. Sensors 2017;17(11):2566. https://doi.org/10.3390/s17112566.

[6] Sony S, Laventure S, Sadhu A. A literature review of next-generation smart sensing technology in structural health monitoring. Struct Control Health Monit 2019;26(3):e2321. https://doi.org/10.1002/stc.2321.

[7] Elahi MMA, Hossain MM, Karim MR, Zain MFM, Shearer C. A review on alkali-activated binders: materials composition and fresh properties of concrete. Constr Build Mater 2020;260:119788. https://doi.org/10.1016/j.conbuildmat.2020.119788.

[8] Huang B-T, Li Q-H, Xu S-L, Zhou B. Strengthening of reinforced concrete structure using sprayable fiber-reinforced cementitious composites with high ductility. Compos Struct 2019;220:940–52. https://doi.org/10.1016/j.compstruct.2019.04.061.

[9] Savino V, Lanzoni L, Tarantino AM, Viviani M. Simple and effective models to predict the compressive and tensile strength of HPFRC as the steel fiber content and type changes. Composites Part B Engineering 2018;137:153–62. https://doi.org/10.1016/j.compositesb.2017.11.003.

[10] Saradar A, et al. Prediction of mechanical properties of lightweight basalt fiber reinforced concrete containing silica fume and fly ash: experimental and numerical assessment. J Build Eng 2020;32:101732. https://doi.org/10.1016/j.jobe.2020.101732.

[11] Qureshi LA, Ali B, Ali A. Combined effects of supplementary cementitious materials (silica fume, GGBS, Fly ash and rice husk ash) and steel fiber on the hardened properties of recycled aggregate concrete. Constr Build Mater 2020;263:120636. https://doi.org/10.1016/j.conbuildmat.2020.120636.

[12] Nedunuri SSSA, Sertse SG, Muhammad S. Microstructural study of portland cement partially replaced with Fly ash, ground granulated blast furnace slag and silica fume as determined by pozzolanic activity. Constr Build Mater 2020;238:117561. https://doi.org/10.1016/j.conbuildmat.2019.117561.

[13] Burhan L, Ghafor K, Mohammed A. Modeling the effect of silica fume on the compressive, tensile strengths and durability of NSC and HSC in various strength ranges. J Build Pathol Rehabil 2019;4:19. https://doi.org/10.1007/s41024-019-0058-4.

[14] Liu Y, Shi C, Zhang Z, Li N, Shi D. Mechanical and fracture properties of ultra-high performance geopolymer concrete: effects of steel fiber and silica fume. Cem Concr Compos 2020;112:103665. https://doi.org/10.1016/j.cemconcomp.2020.103665.

[15] Wu W, Wang R, Zhu C, Meng Q. The effect of Fly ash and silica fume on mechanical properties and durability of coral aggregate concrete. Constr Build Mater 2018;185:69–78. https://doi.org/10.1016/j.conbuildmat.2018.06.097.

[16] Kim J-E, et al. Mechanical properties of energy efficient concretes made with binary, ternary, and quaternary cementitious blends of Fly ash, blast furnace slag, and silica fume. Int J Concr Struct Mater 2016;10(3):97–108. https://doi.org/10.1007/s40069-016-0162-7.

[17] Tripathi M, Dhakal RP, Dashti F. Nonlinear cyclic behaviour of high-strength ductile RC walls: experimental and numerical investigations. Eng Struct 2020;222:111116. https://doi.org/10.1016/j.engstruct.2020.111116.

[18] Falliano D, De Domenico D, Ricciardi G, Gugliandolo E. Improving the flexural capacity of extrudable foamed concrete with glass-fiber bi-directional grid reinforcement: an experimental study. Compos Struct 2019;209:45–59. https://doi.org/10.1016/j.compstruct.2018.10.092.

[19] Müller P, Novák J, Holan J. Destructive and non-destructive experimental investigation of polypropylene fibre reinforced concrete subjected to high temperature. J Build Eng 2019;26:100906. https://doi.org/10.1016/j.jobe.2019.100906.

[20] Feng D-C, et al. Machine learning-based compressive strength prediction for concrete: an adaptive boosting approach. Constr Build Mater 2020;230:117000. https://doi.org/10.1016/j.conbuildmat.2019.117000.

[21] ASTM, Standard test method for compressive strength of cylindrical concrete specimens. ASTM C 2010;39.

[22] ASTM, Standard Test Method for Splitting Tensile Strength of Cylindrical Concrete Specimens. 2017.

[23] Malek J, Kaouther M. Destructive and non-destructive testing of concrete structures. Jordan J Civ Eng 2014;8(4):432–41.

[24] Li G, Gu J, Ren Z, Zhao F, Zhang Y. Damage evaluation of concrete under uniaxial compression based on the stress dependence of AE elastic wave velocity combined with DIC technology. Materials 2021;14(20):6161. https://doi.org/10.3390/ma14206161.

[25] Mishra M, Bhatia AS, Maity D. Predicting the compressive strength of unreinforced brick masonry using machine learning techniques validated on a case study of a museum through nondestructive testing. J Civ Struct Health Monit 2020;10(3):389–403. https://doi.org/10.1007/s13349-020-00391-7.

[26] Razzaghi H, Madandoust R, Aghabarati H. Point-load test and UPV for compressive strength prediction of recycled coarse aggregate concrete via generalized GMDH-class neural network. Constr Build Mater 2021;276:122143. https://doi.org/10.1016/j.conbuildmat.2020.122143.

[27] Asteris PG, Mokos VG. Concrete compressive strength using artificial neural networks. Neural Comput Appl 2020;32(15):11807–26. https://doi.org/10.1007/s00521-019-04663-2.

[28] Ahmad A, et al. Prediction of compressive strength of Fly ash based concrete using individual and ensemble algorithm. Materials 2021;14(4). https://doi.org/10.3390/ma14040794.

[29] Mohammed HRM, Ismail S. Proposition of new computer artificial intelligence models for shear strength prediction of reinforced concrete beams. Eng Comput 2021. https://doi.org/10.1007/s00366-021-01400-z.

[30] Kaloop MR, Kumar D, Samui P, Hu JW, Kim D. Compressive strength prediction of high-performance concrete using gradient tree boosting machine. Constr Build Mater 2020;264:120198. https://doi.org/10.1016/j.conbuildmat.2020.120198.

[31] Hoang N-D, Pham A-D, Nguyen Q-L, Pham Q-N. Estimating compressive strength of high performance concrete with Gaussian process regression model. Adv Civ Eng 2016;2016:2861380. https://doi.org/10.1155/2016/2861380.

[32] Ni T, Zhou R, Gu C, Yang Y. Measurement of concrete crack feature with android smartphone APP based on digital image processing techniques. Measurement 2020;150:107093. https://doi.org/10.1016/j.measurement.2019.107093.

[33] Natesaiyer K, et al. X-ray CT imaging and finite element computations of the elastic properties of a rigid organic foam compared to experimental measurements: insights into foam variability. J Mater Sci 2015;50(11):4012–24. https://doi.org/10.1007/s10853-015-8958-4.

[34] Kim H, Ahn E, Shin M, Sim S-H. Crack and noncrack classification from concrete surface images using machine learning. Struct Health Monit 2019;18(3):725–38. https://doi.org/10.1177/1475921718768747.

[35] Yoshitake I, Maeda T, Hieda M. Image analysis for the detection and quantification of concrete bugholes in a tunnel lining. Case Stud Constr Mater 2018;8:116–30. https://doi.org/10.1016/j.cscm.2018.01.002.

[36] Zhan BJ, Xuan DX, Poon CS, Scrivener KL. Characterization of interfacial transition zone in concrete prepared with carbonated modeled recycled concrete aggregates. Cem Concr Res 2020;136:106175. https://doi.org/10.1016/j.cemconres.2020.106175.

[37] Ahmad A, et al. Comparative study of supervised machine learning algorithms for predicting the compressive strength of concrete at high temperature. Materials 2021;14(15). https://doi.org/10.3390/ma14154222.

[38] Asteris PG, Skentou AD, Bardhan A, Samui P, Pilakoutas K. Predicting concrete compressive strength using hybrid ensembling of surrogate machine learning models. Cem Concr Res 2021;145:106449. https://doi.org/10.1016/j.cemconres.2021.106449.

[39] Kang M-C, Yoo D-Y, Gupta R. Machine learning-based prediction for compressive and flexural strengths of steel fiber-reinforced concrete. Constr Build Mater 2021;266:121117. https://doi.org/10.1016/j.conbuildmat.2020.121117.

[40] Başyiğit C, Çomak B, Kılınçarslan Ş, Serkan Üncü İ. Assessment of concrete compressive strength by image processing technique. Constr Build Mater 2012;37:526–32. https://doi.org/10.1016/j.conbuildmat.2012.07.055.

[41] Dogan G, Arslan MH, Ceylan M. Concrete compressive strength detection using image processing based new test method. Measurement 2017;109:137–48. https://doi.org/10.1016/j.measurement.2017.05.051.

[42] Dogan G, Arslan MH, Ceylan M. Statistical feature extraction based on an ANN approach for estimating the compressive strength of concrete. Neural Netw World 2015;25(3):301. https://doi.org/10.14311/NNW.2015.25.016.

[43] Peng Y, Ying L, Kamel MMA, Wang Y. Mesoscale fracture analysis of recycled aggregate concrete based on digital image processing technique. Struct Concr 2021;22(S1):E33–47. https://doi.org/10.1002/suco.201900338.

[44] Ghanizadeh AR, Abbaslou H, Amlashi AT, Alidoust P. Modeling of bentonite/sepiolite plastic concrete compressive strength using artificial neural network and support vector machine. Front Struct Civ Eng 2019;13(1):215–39. https://doi.org/10.1007/s11709-018-0489-z.

[45] Zhang M, Li M, Shen Y, Ren Q, Zhang J. Multiple mechanical properties prediction of hydraulic concrete in the form of combined damming by experimental data mining. Constr Build Mater 2019;207:661–71. https://doi.org/10.1016/j.conbuildmat.2019.02.169.

[46] Koya BP, Aneja S, Gupta R, Valeo C. Comparative analysis of different machine learning algorithms to predict mechanical properties of concrete. Mech Adv Mater Struct 2021;29(25):4032–43. https://doi.org/10.1080/15376494.2021.1917021.

[47] Zhang Y, Xu X. Predicting multiple properties of pervious concrete through the Gaussian process regression. Adv Civ Eng Mater 2021;10(1):56–73. https://doi.org/10.1520/ACEM20200134.

[48] Yetilmezsoy K, Sihag P, Kıyan E, Doran B. A benchmark comparison and optimization of Gaussian process regression, support vector machines, and M5P tree model in approximation of the lateral confinement coefficient for CFRP-wrapped rectangular/square RC columns. Eng Struct 2021;246:113106. https://doi.org/10.1016/j.engstruct.2021.113106.

[49] Basaran B, Kalkan I, Bergil E, Erdal E. Estimation of the FRP-concrete bond strength with code formulations and machine learning algorithms. Compos Struct 2021;268:113972. https://doi.org/10.1016/j.compstruct.2021.113972.

[50] Imran Waris M, Plevris V, Mir J, Chairman N, Ahmad A. An alternative approach for measuring the mechanical properties of hybrid concrete through image processing and machine learning. Constr Build Mater 2022;328:126899. https://doi.org/10.1016/j.conbuildmat.2022.126899.

[51] Arasan S, Yenera E, Hattatoglu F, Hinislioglua S, Akbuluta S. Correlation between shape of aggregate and mechanical properties of asphalt concrete: digital image processing approach. Road Mater Pavement Des 2011;12(2):239–62. https://doi.org/10.1080/14680629.2011.9695245.

[52] Gouillart E, Nunez-Iglesias J, Van Der Walt S. Analyzing microtomography data with python and the scikit-image library. Adv Struct Chem Imaging 2016;2(1):1–11. https://doi.org/10.1186/s40679-016-0031-0.

[53] Liu Y-F, Cho S, Spencer Jr BF, Fan J-S. Concrete crack assessment using digital image processing and 3D scene reconstruction. J Comput Civ Eng 2016;30(1):04014124. https://doi.org/10.1061/(ASCE)CP.1943-5487.0000446.

[54] Akkoyun O. An evaluation of image processing methods applied to marble quality classification. Proceedings of the 2nd International Conference on Computer Technology and Development. IEEE; 2010. p. 158–62. https://doi.org/10.1109/ICCTD.2010.5646128.

[55] Asteris PG, Koopialipoor M, Armaghani DJ, Kotsonis EA, Lourenço PB. Prediction of cement-based mortars compressive strength using machine learning techniques. Neural Comput Appl 2021;33(19):13089–121. https://doi.org/10.1007/s00521-021-06004-8.

[56] Zhu X, Zhang S, Jin Z, Zhang Z, Xu Z. Missing value estimation for mixed-attribute data sets. IEEE Trans Knowl Data Eng 2010;23(1):110–21. https://doi.org/10.1109/TKDE.2010.99.

[57] Farooq F, Ahmed W, Akbar A, Aslam F, Alyousef R. Predictive modeling for sustainable high-performance concrete from industrial wastes: a comparison and optimization of models using ensemble learners. J Clean Prod 2021;292:126032. https://doi.org/10.1016/j.jclepro.2021.126032.

[58] Le T-T, Le MV. Development of user-friendly kernel-based Gaussian process regression model for prediction of load-bearing capacity of square concrete-filled steel tubular members. Mater Struct 2021;54(2):59. https://doi.org/10.1617/s11527-021-01646-5.

[59] Daniel DG, Lobo CL. User's guide to ASTM specification c 94 on Ready-mixed concrete. ASTM International; 2005. ISBN: 0803133634.

[60] ACI Committee 318, *ACI CODE 318-08: Building Code Requirements for Structural Concrete and Commentary*. American Concrete Institute. p. 473.

[61] ASTM C31/C31M-25a. Standard Practice for Making and Curing Concrete Test Specimens in the Field. 2025. https://doi.org/10.1520/C0031_C0031M-25A.

[62] Öztaş A, et al. Predicting the compressive strength and slump of high strength concrete using neural network. Constr Build Mater 2006;20(9):769–75. https://doi.org/10.1016/j.conbuildmat.2005.01.054.

[63] Yeh IC. Exploring concrete slump model using artificial neural networks. J Comput Civ Eng 2006;20(3):217–21. https://doi.org/10.1061/(ASCE)0887-3801(2006)20:3(217).

[64] Petronas U. Mean and standard deviation features of color histogramusing laplacian filter for content-based image retrieval. J Theor Appl Inf Technol 2011;34(1):1–7.

[65] Sergyan S. Color histogram features based image classification in content-based image retrieval systems. in Proceedings of the 6th International Symposium on Applied Machine Intelligence and Informatics. IEEE; 2008. p. 221–4. https://doi.org/10.1109/SAMI.2008.4469170.

[66] Vapnik VN. he Nature of Statistical Learning Theory. Springer science & business media; 2000. https://doi.org/10.1007/978-1-4757-3264-1. ISBN: 978-0-387-98780-4.

[67] Ahmadi MH, Ahmadi MA, Sadatsakkak SA, Feidt M. Connectionist intelligent model estimates output power and torque of stirling engine. Renew Sustain Energy Rev 2015;50:871–83. https://doi.org/10.1016/j.rser.2015.04.185.

[68] Ahmadi MH, Ahmadi MA, Nazari MA, Mahian O, Ghasempour R. A proposed model to predict thermal conductivity ratio of Al2O3/EG nanofluid by applying least squares support vector machine (LSSVM) and genetic algorithm as a connectionist approach. J Therm Anal Calorim 2019;135(1):271–81. https://doi.org/10.1007/s10973-018-7035-z.

[69] Ahmadianfar I, Jamei M, Karbasi M, Sharafati A, Gharabaghi B. A novel boosting ensemble committee-based model for local scour depth around non-uniformly spaced pile groups. Eng Comput 2021. https://doi.org/10.1007/s00366-021-01370-2.

[70] Schapire RE. The strength of weak learnability. Mach Learn 1990;5(2):197–227. https://doi.org/10.1007/BF00116037.

[71] Breiman L. Bagging predictors. Mach Learn 1996;24(2):123–40. https://doi.org/10.1007/BF00058655.

[72] Saleem MS, Khan MJ, Khurshid K, Hanif MS. Crowd density estimation in still images using multiple local features and boosting regression ensemble. Neural Comput Appl 2020;32(21):16445–54. https://doi.org/10.1007/s00521-019-04021-2.

[73] Van Heijst D, Potharst R, van Wezel M. A support system for predicting ebay end prices. Decis Support Syst 2008;44(4):970–82. https://doi.org/10.1016/j.dss.2007.11.004.

[74] Plevris V, Solorzano G, Bakas NP, Ben Seghier MEA. Investigation of performance metrics in regression analysis and machine learning-based prediction models. Oslo, Norway: ECCOMAS; 2022. https://doi.org/10.23967/eccomas.2022.155.